

# Simulation study for ground-based Ku-band microwave observations of ozone and hydroxyl in the polar middle atmosphere

David A. Newnham<sup>1</sup>, Mark A. Clilverd<sup>1</sup>, Michael Kosch<sup>2,3</sup>, Annika Seppälä<sup>4</sup>, and Pekka T. Verronen<sup>5</sup>

<sup>1</sup>British Antarctic Survey (BAS), High Cross, Madingley Road, Cambridge, CB3 0ET, United Kingdom.

5 <sup>2</sup>Physics Department, Lancaster University, Lancaster, LA1 4YB, United Kingdom.

<sup>3</sup>South African National Space Agency (SANSA), Hospital Street, Hermanus 7200, South Africa.

<sup>4</sup>Department of Physics, University of Otago, PO Box 56, Dunedin 9054, New Zealand.

<sup>5</sup>Space and Earth Observation Centre, Finnish Meteorological Institute, Helsinki, Finland.

*Correspondence to:* David A. Newnham (dawn@bas.ac.uk)

10 **Abstract.** The Ku-band microwave frequencies (10.70–14.25 GHz) overlap emissions from ozone (O<sub>3</sub>) at 11.072 GHz and hydroxyl radical (OH) at 13.441 GHz. These important chemical species in the polar middle atmosphere respond strongly to high-latitude geomagnetic activity associated with space weather. Atmospheric model calculations predict that energetic electron precipitation (EEP) driven by magnetospheric sub-storms produces large changes in polar mesospheric O<sub>3</sub> and OH. The EEP typically peaks at geomagnetic latitudes ~65° and evolves rapidly with time longitudinally and over the geomagnetic  
15 latitude range 60°–80°. Previous atmospheric modelling studies have shown that during sub-storms OH abundance can increase by more than an order of magnitude at 64–84 km and mesospheric O<sub>3</sub> losses can exceed 50%. In this work, an atmospheric simulation and retrieval study has been performed to determine the requirements for passive microwave radiometers capable of measuring diurnal variations in O<sub>3</sub> and OH profiles from high-latitude northern hemisphere and Antarctic locations to verify model predictions. We show that, for a 11.072 GHz radiometer making 6 h spectral measurements  
20 with 10 kHz frequency resolution and root-mean-square baseline noise of 1 mK, O<sub>3</sub> could be profiled over 8×10<sup>-4</sup>–0.22 hPa (~98–58 km) with 10–17 km height resolution and ~1 ppmv uncertainty. For the equivalent 13.441 GHz measurements with vertical sensor polarisation, OH could be profiled over 3×10<sup>-3</sup>–0.29 hPa (~90–56 km) with 10–17 km height resolution and ~3 ppbv uncertainty. The proposed observations would be highly applicable to studies of EEP, atmospheric dynamics, planetary-scale circulation, chemical transport, and the representation of these processes in polar and global climate models.  
25 Such observations would provide a relatively low-cost alternative to increasingly sparse satellite measurements of the polar middle atmosphere, extending long-term data records and also providing “ground truth” calibration data.

## 1 Introduction

### 1.1 Background information

Energetic particle precipitation (EPP) is an important mechanism in the polar middle and upper atmosphere, causing ionisation  
30 in the neutral atmosphere and producing odd nitrogen (NO<sub>x</sub> = NO + NO<sub>2</sub>) and odd hydrogen (HO<sub>x</sub> = OH + HO<sub>2</sub>) (Brasseur

and Solomon, 2005; Mironova et al., 2015; Sinnhuber et al., 2012; Verronen and Lehmann, 2013). Enhanced abundances of these chemical species lead to catalytic destruction of ozone ( $O_3$ ) (Jackman and McPeters, 2004), perturbing the radiative balance, dynamics, and large scale circulation patterns of the atmosphere. This mechanism potentially links solar variability associated with space weather to regional surface climate (e.g. Arsenovic et al., 2016; Baumgartner et al., 2011; Semeniuk et al., 2011; Seppälä et al., 2009, 2013). The energetic particles, mainly protons and electrons of solar and magnetospheric origin, vary widely in energy range and the regions of the atmosphere where they impact, both in geographic/geomagnetic coverage and altitude. Energetic electron precipitation (EEP), with electron energies in the range 20–300 keV, increases ionization in the polar mesosphere at altitudes of 60–90 km (Newnham et al., 2018; Turunen et al., 2009).

Atmospheric model calculations (Seppälä et al., 2015) predict that EEP driven by magnetospheric sub-storms produces large changes in polar mesospheric  $O_3$  and  $HO_x$ . The EEP typically peaks at geomagnetic latitudes  $\sim 65^\circ$  (e.g. Kilpisjärvi, Finland and Syowa station, Antarctica) and evolves rapidly with time eastwards and over the geomagnetic latitude range  $60^\circ$ – $80^\circ$  (Cresswell-Moorcock et al., 2013). During the sub-storms the modelled night-time OH partial column over the altitude range 64–84 km can increase by more than 1000% and the OH volume mixing ratio (VMR) at 70 km increases from the background (i.e. no sub-storm) level of  $\sim 8$  ppbv to  $\sim 60$  ppbv (Seppälä et al., 2015). The sub-storms leave footprints of 5–55% mesospheric  $O_3$  loss lasting many hours of local time, with strong altitude and seasonal dependences (Seppälä et al., 2015). The cumulative atmospheric response of  $\sim 1250$  sub-storms.yr $^{-1}$  (Rodger et al., 2016) is potentially more important than the impulsive but highly sporadic ( $\sim 3$ – $4$ /year) effects of solar proton events. Other recent studies suggest that EEP from the Earth's outer radiation belt continuously affects the composition of the polar mesosphere through  $HO_x$ -driven chemistry (Andersson et al., 2014a), and that  $HO_x$  may cause prolonged mesospheric  $O_3$  depletion when  $NO_x$  is enhanced during polar winter (Verronen and Lehmann, 2015). Mesospheric OH is predominantly produced by the photo-dissociation of water vapour ( $H_2O$ ) and  $HO_x$  measurements can also be used as a proxy for mesospheric  $H_2O$  (Summers et al., 2001). In order to test, verify, and improve models of the polar stratosphere and mesosphere,  $O_3$  and OH observations are needed with sufficient precision and time resolution to characterise the different processes that modify their chemical abundances. This paper identifies the instrument characteristics that would be needed to produce the required observations.

## 25 **1.2 Previous mesospheric ozone and hydroxyl measurements**

$O_3$  vertical profiles retrieved in the upper mesosphere (70–100 km) from observations by nine recently-operating satellite instruments have been reviewed and compared (Smith et al., 2013). The comparison of coincident profiles showed that upper mesospheric ozone is abundant during the night and depleted during the day, the secondary  $O_3$  VMR maximum occurs at 90–92 km during the day and 95 km at night, and  $O_3$  VMR is very low ( $< 0.2$  ppmv) at about 80 km during both day and night with a minimum in ozone density at sunrise at 80 km. The Microwave Limb Sounder (MLS) on the Aura satellite has provided a long time series of stratospheric and mesospheric  $O_3$  measurements (Froidevaux et al., 2008) with global coverage, although the precision of retrieved  $O_3$  profiles decreases sharply above 0.1 hPa ( $\sim 64$  km). MLS observations of mesospheric OH (Pickett et al., 2008) have also helped to elucidate the role of different types of EEP in polar  $O_3$  variability (e.g., Andersson et

al., 2014b; Verronen et al., 2011; Zawedde et al., 2018). Minschwaner et al. (2011) reviewed OH in the stratosphere and mesosphere and used MLS data to study its diurnal variability. The Spatial Heterodyne Imager for Mesospheric Radicals (SHIMMER) (Englert et al., 2010) measured OH diurnal variations for investigations into discrepancies in mesospheric HO<sub>x</sub> in photochemical models that had been suggested by earlier satellite observations (Siskind et al., 2013). A major limitation of satellite observations is that the temporal and spatial sampling arising from several overpasses per day at polar locations can make investigating rapidly-evolving, short term, chemical changes, such as those induced by sub-storms, a challenge.

Ground-based millimetre-wave radiometry at 110–250 GHz provides continuous measurements of O<sub>3</sub> (e.g., Hartogh et al., 2004; Daae et al., 2014; Ryan et al., 2016) and perhydroxyl radical (HO<sub>2</sub>) (Clancy et al., 1994) but the altitude range is typically restricted to ~20–75 km. Above ~75 km, thermal Doppler broadening increases and lower pressure / higher altitude information cannot be retrieved from the emission lines. However, for the O<sub>3</sub> microwave line centred at 11.072 GHz the atmosphere is much less opaque and Doppler broadening is 10–23 times lower than at 110–250 GHz, allowing the retrieval of O<sub>3</sub> VMR to higher altitudes. Low cost, ground-based microwave radiometers operating at 11.072 GHz have been developed using inexpensive Ku-band satellite television low noise block (LNB) downconverters (Rogers et al., 2009; Rogers et al., 2012). Applying a straightforward processing scheme, O<sub>3</sub> partial columns for the lower mesosphere (~50–80 km) and the upper mesosphere / lower thermosphere (~80–100 km) have been determined from the central 1.25 MHz section of observed 11.072 GHz O<sub>3</sub> spectra. The current observations can broadly estimate seasonal O<sub>3</sub> variability near the mesopause but would not readily resolve the altitude-dependent O<sub>3</sub> changes at 60–90 km that are predicted to occur with sub-storms. Furthermore, due to the weakness of the 11.072 GHz emission line, measurement times extend to days using a single receiver radiometer achieving a root mean square (rms) noise level (1 $\sigma$ ) of 5 mK at 9.8 kHz resolution and with 24 h signal integration.

Remote sensing measurements of mesospheric OH abundances from the ground are challenging due to the low VMR, which typically peaks in the ppbv range at ~80 km. Ground-based LIDARs at mid-latitude sites have detected and identified OH in the ground vibrational state, X<sup>2</sup>Π (v' = 0), in the mesosphere at ~75–85 km altitude (Brinksma et al., 1998). The LIDAR measurements detect UV resonant fluorescence at ~308 nm from the OH A<sup>2</sup>Σ – X<sup>2</sup>Π electronic transition. In contrast, near-infrared and visible airglow emissions in the X<sup>2</sup>Π ro-vibrational Meinel system are due to deactivation of vibrationally-excited OH\* (v' = 7 to v' = 9) generated by the highly exothermic reaction of atomic hydrogen with O<sub>3</sub>. Satellite measurements of Meinel band night-glow have shown that OH\* occurs in a ~8 km thick layer near 90 km (Zhang and Shepherd, 1999). Ground-based spectroscopic measurements of individual OH vibrational bands in the Meinel emissions can be used to infer temperatures at the mesopause region and estimate relative populations of the v' states (e.g., von Zahn et al., 1987; Yee et al., 1997; Smith et al., 2010).

### 30 1.3 This work

In this work we investigate the potential for measuring diurnal variations in the vertical profiles of O<sub>3</sub> in the mesosphere and lower thermosphere using the 11.072 GHz emission line, and extending the ground-based microwave radiometry technique to mesospheric OH emissions at ~13.4 GHz. The microwave spectrum of the most abundant hydroxyl isotopomer, <sup>16</sup>OH, at

13.433–13.442 GHz shows four closely-spaced lines which arise from the  $\Lambda$ -doubling hyperfine structure in the rotational  $^2\Pi_{3/2}$  ( $v = 0$ ,  $J = 7/2$ ) state (Radford, 1961; Sastry and Vanderlinde, 1980). The atmospheric OH spectrum is further complicated by the magnetic Zeeman effect, due to the molecule's non-zero total electron spin quantum number ( $S = 1/2$ ). Each line is Zeeman split into several components polarised in a quasi-symmetric manner and shifted from the central  
5 frequency. Here we investigate potential measurements using the most intense of the four OH rotational lines, which has a line position of 13.441 GHz.

The study focuses on atmospheric simulations and retrievals for Kilpisjärvi, Finland, since model data for  $O_3$  and OH abundances in sub-storm and background (no sub-storm) conditions are available for this location. However, we demonstrate the technique's wider applicability by comparing atmospheric microwave transmittances at six land-based locations including  
10 Kilpisjärvi, shown on the maps in Figure 1. Three potential sites for ground-based instruments are in the Antarctic and three are at high-latitude in the northern hemisphere (NH), and all are located close to geomagnetic latitude  $65^\circ$  where sub-storms are predicted to have the greatest effect on mesospheric  $O_3$  and OH.

## 2 Methodology

Microwave spectrum simulations and retrievals have been performed using atmospheric model data-sets in radiative transfer  
15 calculations for selected high-latitude and polar locations. The synthesis of VMR profiles at these locations for  $O_3$ , OH, and seven other atmospheric species, as well as temperature profiles, from available model data is described in Section 2.1. The configuration of the radiative transfer forward model for simulating clear-sky atmospheric microwave transmittance and brightness temperature spectra is given in Section 2.2, and the setups for performing  $O_3$  and OH retrievals for Kilpisjärvi, Finland are given in Section 2.3.

### 20 2.1 Atmospheric model datasets

Nine chemical species were identified as significant contributors to the clear-sky atmospheric microwave spectrum in the 11–14 GHz region, overlapping the target  $O_3$  and OH lines at 11.072 GHz and 13.441 GHz: ozone ( $O_3$ ), hydroxyl radical (OH), water vapour ( $H_2O$ ), molecular nitrogen ( $N_2$ ), molecular oxygen ( $O_2$ ), perhydroxyl radical ( $HO_2$ ), nitric acid ( $HNO_3$ ), hydrogen peroxide ( $H_2O_2$ ), and carbon dioxide ( $CO_2$ ). Monthly mean vertical profiles of VMR for the atmospheric species, and  
25 temperature, were calculated using a 10-year dataset from WACCM-D (Verronen et al., 2016) covering 2000–2009. WACCM-D is a 3-D global atmospheric model that incorporates a detailed representation of  $D$ -region chemistry in the specified dynamics (SD) version of the Whole Atmosphere Community Climate Model (WACCM 4) (Marsh et al., 2013). The model data were taken from the WACCM-D longitude / latitude grid points closest to the six locations of interest. Seasonal winter mean profiles were calculated using December, January, and February (DJF) data for the NH locations and June, July,  
30 and August (JJA) data for the southern hemisphere (SH). Similarly, summer mean profiles were calculated using JJA data for the NH locations and DJF data for the SH locations.

O<sub>3</sub> and OH VMR profiles for sub-storm and background (no sub-storm) conditions were computed by combining data from the 1-D Sodankylä Ion and Neutral Chemistry (SIC) model (Verronen et al., 2005) with monthly-mean WACCM-D data. The SIC model data provided VMR data over the altitude range 20–100 km and monthly-mean data from WACCM-D filled the region from the ground up to 20 km and above 100 km. Figure 2(a) shows O<sub>3</sub> number density profiles calculated using a 9-day SIC model run (Seppälä et al., 2015) for December 2007 with sub-storm conditions at Kilpisjärvi. The largest decreases in mesospheric O<sub>3</sub> abundance, exceeding 50%, occur over the altitude range 68–86 km during a four-day period, after which the number densities return to background levels (Figure 2(b)). The percentage changes in O<sub>3</sub> partial column over altitudes 64–84 km for the original (15 min) model resolution and 1 h, 6 h, and 24 h moving average smoothed data are shown in Figure 2(c). The three smoothed datasets show reduced diurnal variability compared to the original model data but the largest decrease in O<sub>3</sub> partial column is little changed by averaging up to 24 h. VMR profiles for sub-storm and background (no sub-storm) conditions were determined from the SIC model data coincident with the largest decrease in O<sub>3</sub> partial column, and these and the monthly-mean profiles are shown in Figure 2(d). Sub-storm reductions in O<sub>3</sub> VMR occur over the altitude range 64–94 km, with the largest decrease at 72 km.

A similar approach was used to determine OH VMR profiles, as shown in Figure 3. The largest increases in mesospheric OH abundance, exceeding two orders of magnitude above the background level, occur at altitudes in the range 66–82 km during the four days corresponding to O<sub>3</sub> decreases, after which OH number densities return to background levels (Figures 3(a) and 3(b)). The percentage changes in OH partial column over altitudes 64–84 km for the original (15 min) model resolution and 1 h, 6 h, and 24 h moving averages are shown in Figure 3(c). The enhanced level of mesospheric OH during sub-storms shows greater diurnal variability than the corresponding O<sub>3</sub> reductions. Smoothing the modelled OH partial columns significantly reduces the daily maxima, indicating that the improved signal-to-noise from atmospheric measurements longer than ~6 h would be strongly offset by the smaller integrated OH signal. The 6-h smoothed sub-storm and background (no sub-storm) VMR profiles corresponding to the largest decrease in OH partial column, and monthly-mean profiles, are shown in Figure 3(d). The sub-storm profile shows a five-fold increase in OH VMR around 82 km compared to the monthly-mean and background (no sub-storm) data.

## 2.2 Forward modelling of atmospheric spectra

Simulated atmospheric microwave spectra were calculated using version 2.2.58 of the Atmospheric Radiative Transfer Simulator (ARTS) (available at <http://www.radiativetransfer.org/>) (Buehler et al., 2005; Buehler et al., 2018; Eriksson et al., 2011) and the Qpack2 (a part of atmlab v2.2.0) software package (Eriksson et al., 2005). ARTS is a monochromatic line-by-line model that can simulate radiances from the infrared to the microwave and has been validated against other models in the submillimetre spectral range (Melsheimer et al., 2005). The model includes contributions from spectral lines and broadband continua via a choice of user-specified parameterisations. The Planck formalism was used for calculating brightness temperatures and atmospheric transmittance.

Spectroscopic line parameters for O<sub>3</sub>, OH, H<sub>2</sub>O, N<sub>2</sub>, O<sub>2</sub>, HO<sub>2</sub>, HNO<sub>3</sub>, H<sub>2</sub>O<sub>2</sub>, and CO<sub>2</sub> were taken from the high-resolution transmission (HITRAN) molecular absorption database (Gordon et al., 2017). For all molecules except OH the Kuntz approximation (Kuntz, 1997) to the Voigt lineshape was used with a Van Vleck–Huber prefactor (Van Vleck and Huber, 1977) and a line cut-off of 750 GHz which is valid for the pressures considered. As the water vapour continuum parameterisation the Mlawer–Tobin Clough–Kneizys–Davies (MT-CKD) model (version 2.5.2) was used, which includes both foreign and self-broadening components (Mlawer et al., 2012). Collision-induced absorption (CIA) is the main contribution to the dry continua in the microwave range, and therefore the CIA parameterisations from the MT-CKD model (Clough et al., 2005) (version 2.5.2 for N<sub>2</sub> and CO<sub>2</sub> and version 1.0 for O<sub>2</sub>) were applied.

In order to compare seasonal atmospheric transmittances at the six different locations, survey spectra over the frequency range 5–20 GHz were calculated at zenith angles of 0° and 82° using mean winter and mean summer profiles. A 1 MHz frequency grid was chosen, adequate to characterise smoothly varying, broadband transmittance but insufficient to resolve narrow-band spectral features.

For simulations of ground-based microwave measurements, values for the frequency resolution, bandwidth, and baseline noise were chosen by considering the range of atmospheric emission linewidths and likely instrument performance. Pressure-broadened, Doppler-broadened, and Voigt full-width half-maxima (FWHM) linewidths for the lines were calculated using air-broadening coefficients from HITRAN and winter (DJF) and summer (JJA) pressure and temperature profiles at Kilpisjärvi. Figures 4(a) and 4(b) show the variation of O<sub>3</sub> 11.072 GHz and OH 13.441 GHz linewidths with altitude. For both molecules pressure-broadening dominates below ~90 km, increasing rapidly below 85 km to give FWHM linewidths of 300 kHz at ~65–70 km in winter and ~70–75 km in summer. Voigt linewidths are lowest in the lower thermosphere at ~95–100 km, with minimum FWHM of 17 kHz for O<sub>3</sub> and 34 kHz for OH, and increase above 100 km due to increased Doppler broadening. Forward model spectra were therefore calculated with a frequency grid spacing of 10 kHz over a bandwidth of 1 MHz to encompass the range of emission linewidths from O<sub>3</sub> and OH in the mesosphere and lower thermosphere. All measurement simulations were performed for a single pencil beam of radiation at a zenith angle of 82°.

An important consideration in our calculations is that O<sub>3</sub> and OH atmospheric spectra can be measured over 6 h with rms baseline noise of 1.0 mK, and this assumption is justified as follows. Low-cost LNB receivers with noise factor ~1.3 dB currently used in O<sub>3</sub> 11.072 GHz spectrometers for the educational project Mesospheric Ozone System for Atmospheric Investigations in the Classroom (MOSAIC) operate uncooled, i.e. at ambient temperature (Rogers et al., 2012). By analysing signals from both horizontal and vertical polarisation channels of the LNB with 10 kHz frequency resolution, and integrating the atmospheric signal for 24 h, an atmospheric spectrum with baseline noise of ~3.4 mK is achieved. The statistical fluctuation  $\Delta T$  (K) in the total system temperature,  $T_{sys}$  (K), is calculated according to the ideal radiometer equation (Kraus, 1986):

$$\Delta T = \frac{T_{sys}}{\sqrt{t\Delta f N_{CH}}} \quad (1)$$

where  $t$  is observation time (in s),  $\Delta f$  is the frequency resolution (in Hz) of the radiometer, and  $N_{CH}$  is the number of measurement channels. Applying this equation we can define the sensor characteristics needed to achieve a signal-to-noise of 1.0 mK in 6 h measurements, providing adequate time resolution to observe predicted changes in mesospheric O<sub>3</sub> and OH. The results in Table 1 show that higher performance LNB receivers, with noise factor 0.7 dB, would achieve such measurements of the O<sub>3</sub> 11.072 GHz emission if cooled to 168 K. Alternatively an array of 12 receivers operating at room temperature, with a total of 24 measurement channels, would achieve this measurement performance. At the higher frequency (13.441 GHz) of the OH emission available LNBs are less sensitive, with noise factor 1.2 dB, and would require cryogenic operation at 46 K to achieve the equivalent performance. A receiver array at room temperature would need 40 spectrometers (i.e. 80 measurement channels) to achieve the required measurement performance at 13.441 GHz. Thus we conclude that suitable receivers could be constructed using commercially-available LNB receivers, albeit with the added complexity and higher power consumption needed for low-temperature operation or, alternatively, by combining the outputs from multiple room temperature receivers to achieve higher signal-to-noise spectra.

The treatment of the Zeeman effect in the Stokes formalism of ARTS is described by Larsson et al. (2014). The Zeeman components of the OH line centred at 13.441 GHz were calculated for an instrument viewing at an azimuthal angle 0° i.e., northward-looking from Kilpisjärvi, with sensor polarisation either vertical, horizontal, or in both directions combined. Magnetic field data were taken from IGRF-11 (Finlay et al., 2010) and the Faddeeva function was used to describe the lineshape.

Forward model spectra were calculated for ground-based, clear-sky observations during December sub-storm and background (no sub-storm) conditions at Kilpisjärvi. The emission signals from different altitudes were found by selectively setting O<sub>3</sub> and OH VMR to zero for 10 km sections of the mesosphere and lower thermosphere, and also running simulations with zero O<sub>3</sub> and OH VMR at all altitudes. In order to assess measurement uncertainties in the retrieval algorithm and its ability to reproduce the “true” state of the atmosphere, two sets of 500 spectra each of O<sub>3</sub> and OH were calculated for Monte Carlo (MC) error analysis. In one set of MC repeat spectra all VMR profiles were kept constant at the “true” values whereas in the other set the O<sub>3</sub>, OH, and H<sub>2</sub>O profiles were randomly scaled using a uniform distribution over the range 0.5–2.0. Baseline noise with rms level 1.0 mK was randomly calculated and added to each individual O<sub>3</sub> and OH spectrum in both of the MC sets.

### 2.3 Retrievals

The 6 h atmospheric spectra, simulated for December sub-storm and background (no sub-storm) conditions at Kilpisjärvi, were inverted into altitude profiles of O<sub>3</sub> and OH VMR using the optimal estimation method (OEM) (Rodgers, 2000) implemented in Qpack (Eriksson et al., 2005). Iterative absorption calculations in ARTS were performed line-by-line within the radiative transfer calculation, rather than using pre-calculated look-up tables, in order to accurately model atmospheric spectra (Buehler et al., 2011). VMR values were retrieved for altitude levels 0–120 km with a 1 km spacing, where hydrostatic equilibrium was assumed for the altitude and pressure. The O<sub>3</sub>, OH, and H<sub>2</sub>O a priori VMR profiles were the December monthly mean profiles for Kilpisjärvi. The diagonal elements in the covariance of the O<sub>3</sub> and OH a priori were fixed to 1.5 ppmv and 10 ppbv

respectively whereas for H<sub>2</sub>O they were fixed at the square of 50% of the VMR values. The off-diagonal elements of the covariance linearly decrease with a correlation length of a fifth of a pressure decade (approximately 3 km).

### 3 Results

#### 3.1 Simulated atmospheric spectra

5 Survey clear-sky atmospheric transmittance spectra, calculated for the selected locations, are shown in Figure 5. Water vapour absorption leads to decreased transmittance at frequencies above 10 GHz. Higher transmittance occurs for the three colder, desiccated Antarctic sites whereas the generally milder NH locations have lower transmittance especially in summertime. Considering the frequencies of the O<sub>3</sub> and OH lines, at zenith angle 0°, transmittance is 0.98 at the six locations in both winter and summer conditions. At a zenith angle 82° the lower transmittance, in the range 0.84–0.86, is due to the higher air mass  
10 factor and increased tropospheric attenuation in particular by water vapour, oxygen, and nitrogen continua. However, the very similar transmittances at various locations suggest that the different seasonal meteorology should have little impact on the proposed O<sub>3</sub> and OH observations, unlike ground-based measurements using higher frequencies in the millimetre-wave region where cold, dry, high-altitude sites are advantageous.

Forward model simulations of the O<sub>3</sub> 11.072 GHz emission line are shown in Figures 6(a) and 6(b), for the sub-storm and  
15 background (no sub-storm) cases respectively. The solid black lines in each plot are the brightness temperature spectra that would be observed at the ground in clear-sky conditions at a zenith angle of 82°. The other lines show the contributions to the total signal from 10 km layers in the mesosphere and lower thermosphere between 50 km and 110 km. For the sub-storm scenario, O<sub>3</sub> emission is reduced around the peak at 11.072 GHz compared to the background case. The largest decrease in signal corresponds to altitudes 70–80 km, where the modelled reduction in O<sub>3</sub> number density during sub-storms is greatest,  
20 with smaller decreases at 60–70 km and 80–90 km.

Forward model simulations of the OH 13.441 GHz emission line are shown in Figures 7(a)–(f). Figures 7(a), 7(c), and 7(e) are the sub-storm spectra for three different sensor polarisations: - both polarisations, vertical, and horizontal respectively. Figures 7(b), 7(d), and 7(f) show the corresponding spectra for the background (no sub-storm) case. The solid black lines in  
25 each plot are the brightness temperature spectra that would be observed at the ground in clear-sky conditions at a zenith angle of 82°. The other lines are the contribution to the total signal from 10 km layers in the mesosphere and lower thermosphere between 50 km and 100 km. At azimuthal angle 0° the vertical polarisation signal is dominated by a single line centred at 13.441 GHz whereas in horizontal polarisation the pair of Zeeman split lines are clearly resolved. For the sub-storm scenario, OH emission increases around the peak positions compared to the background case. As for O<sub>3</sub>, the largest changes in signal corresponds to altitudes 70–80 km, where the modelled increase in OH number density during sub-storms is greatest, with  
30 smaller increases at 80–90 km.

### 3.2 Ozone retrievals

Example retrieval results are shown in Figure 8 and Figure 9 for simulated clear-sky 6 h observations of the O<sub>3</sub> 11.072 GHz line at 82° zenith angle from Kilpisjärvi in December sub-storm and background conditions using a radiometer providing 10 kHz frequency resolution. Figures 8a and 8e show the final retrieval fits, for the sub-storm and background cases respectively, which agree with the simulated atmospheric spectra to within the rms baseline noise level. Figures 8c and 8g compare the true and a priori O<sub>3</sub> VMR profiles with the retrieved profiles for the sub-storm and background cases respectively. The solid red lines and shaded red areas show the average and standard deviations of the retrieved profiles from 500 repeat MC runs with the O<sub>3</sub> and H<sub>2</sub>O profiles used to calculate the spectra, shown by the dashed blue lines, kept constant at the “true” model values. For both the sub-storm and background cases the retrieved O<sub>3</sub> profiles converge close to the “true” profiles over the altitudes where information is obtained from the observations, shown by the thicker solid lines and shaded grey areas. The description of how the retrieval altitude range is determined is given in the next paragraph. The differences between the retrieved and “true” VMR profiles, shown in Figures 8d and 8h, are in the range -1.0 – 0.6 ppmv. Above and below the retrieval range the O<sub>3</sub> profiles tend towards the a priori values.

The averaging kernels (AVKs) for every sixth retrieved altitude are shown in Figure 9a. The AVKs describe the relationship between the true, a priori, and retrieved atmospheric states (Rodgers, 2000). None of the AVKs peak at pressure levels above 0.0013 hPa (~94 km) due to Doppler broadening dominating over pressure broadening. The lowest AVK peaks are at 0.18 hPa (~60 km). The sum of the AVKs at each altitude, called the measurement (or total) response (MR), represents the extent to which the measurement contributes to the retrieval solution as compared to the influence of the a priori at that altitude (Christensen and Eriksson, 2013). The altitude range where the retrieved O<sub>3</sub> profile has a high degree of independence from the a priori is identified by MR values higher than 0.8. The retrieval altitude range is  $8 \times 10^{-4}$ –0.22 hPa (~98–58 km), shown by the thicker sections of the lines and the shaded grey areas in Figure 8 and Figure 9. Outside of these altitudes (i.e. below 58 km and above 98 km) the MR weakens and the O<sub>3</sub> values in these regions should be interpreted with caution as the information from the a priori becomes important. The AVKs indicate the range of altitudes over which O<sub>3</sub> is observed. In the ideal case the AVKs would be delta functions but in practice they are peaked functions with finite widths dependent on the spatial resolution of the observing system. The full-width half-maximum (FWHM) widths of the kernels provide a measure of the vertical resolution of the retrieved profile. The FWHM values shown in Figure 9b indicate altitude resolutions decreasing from 10.9 km in the lower mesosphere to 18.4 km in the upper mesosphere and lower thermosphere, at altitudes below 98 km. The altitude resolution can also be estimated from the degrees of freedom for signal (DOFS) for the inversion, given by the trace of the AVK matrix (Rodgers, 2000; Ryan and Walker, 2015). Dividing the retrieved altitude range (~30 km) by the DOFS over the same range (~3.2) gives an altitude resolution of 12.0 km, similar to that obtained from the AVK FWHM values.

The OEM calculations provide observation errors ( $\sigma_{obs}$ ) and total retrieval (observation plus smoothing) errors ( $\sigma_{tot}$ ) which provide further diagnostic uncertainty estimates of the retrieved profiles. The observation errors describe how the retrieved

profiles are affected by measurement noise and are shown in Figure 9c, with typical values of about 0.34 ppmv. The observation errors are small outside of the range of the AVK peaks as the retrieval tends to the a priori values in these regions and the contribution from the measurement is small. The total retrieval errors shown in Figure 9d are in the range 1.09–1.34 ppmv, and tend towards the smaller a priori standard deviations outside the range of AVK peaks.

5 The results of the MC error analysis using retrievals from 500 simulated spectra in which O<sub>3</sub> and H<sub>2</sub>O profiles were randomly scaled using a uniform distribution over the range 0.5–2.0, to test the retrieval algorithm’s ability to reproduce the “true” state of the atmosphere, are shown in Figure 9e–f. Over the trustable altitude range the mean difference ( $\mu_{MC}$ ) between the MC retrieved and “true” profiles is in the range -0.8–2.0 ppmv. The standard deviation ( $\sigma_{MC}$ ) of the individual retrievals is an estimator for the uncertainty of the O<sub>3</sub> retrieval, and the mean value of 0.8 ppmv is approximately double the mean observation error determined from single retrievals ( $\sigma_{obs}$ ). Both parameters depend on the signal-to-noise ratio of the input spectrum but  $\sigma_{MC}$  may more realistically represent actual observations where mesospheric O<sub>3</sub> profiles and column H<sub>2</sub>O show large variability.

The Jacobian and gain matrices of the O<sub>3</sub> forward model indicate that an instrument with 10 kHz frequency resolution will adequately sample the emission line for altitudes up to ~98 km where the O<sub>3</sub> measurement contributes significantly to the retrieval. The values of the Jacobian, normalised by the layer thickness of the retrieval grid for observations at an 82° zenith angle, are shown in Figure 10. Typical values of the Jacobian are ~0.5 mK (ppmv)<sup>-1</sup>km<sup>-1</sup> at mesospheric altitudes of 60–90 km where sub-storms are predicted to have the largest effect on O<sub>3</sub> abundance. The effect of predicted O<sub>3</sub> changes of ~1 ppmv over altitudes 68–86 km on the measured atmospheric brightness temperature will therefore be small, of the order of 9 mK close to the emission line centre, but readily measurable with a baseline noise of 1 mK for a 6-hour integration.

### 20 3.3 Hydroxyl (OH) retrievals

Example retrieval results are shown in Figure 11 and Figure 12 for simulated clear-sky 6 h observations of the OH 13.441 GHz line at 82° zenith angle and 0° azimuthal angle from Kilpisjärvi in December sub-storm conditions using a radiometer providing 10 kHz frequency resolution with vertical sensor polarisation. Similar results were obtained for retrievals with simulated spectra using sensors measuring horizontal or both polarisations, and with non-zero azimuthal angles. Figures 11a and 11b show the final retrieval fits which agree with the simulated atmospheric spectra to within the rms baseline noise level. Figures 11c and 11d compare the true sub-storm and a priori OH VMR profiles with the retrieved profiles. The solid red lines and shaded red areas show the average and standard deviation of the retrieved profiles from 500 repeat MC runs with the OH and H<sub>2</sub>O profiles used to calculate the spectra, shown by the dashed blue lines, kept constant at the “true” model values. The retrieved OH profile approaches the “true” profiles over the altitudes where information is obtained from the observations, shown by the thicker solid lines and shaded grey areas. However, Figure 11d shows significant differences, in the range -13.6–3.3 ppbv, between the retrieved and “true” VMR profiles at altitudes which overlap the OH enhancements. Convolution of the true OH profile with the averaging kernels, to account for the limited retrieval resolution, results in much better agreement

with differences (R-T\*) in the range -1.4–2.9 ppbv. Above and below the retrieval range the OH profiles approach the a priori OH VMR values which are close to zero.

The averaging kernels (AVKs) for every sixth retrieved altitude are shown in Figure 12a. None of the AVKs peak at pressure levels above 0.003 hPa (~88 km) due to Doppler broadening dominating over pressure broadening. The lowest AVK peaks at 5 0.24 hPa (~58 km). The estimated retrieval range, where the MR is larger than 0.8, is  $3 \times 10^{-3}$ –0.29 hPa (~90–56 km), shown by the thicker sections of the lines and the shaded grey areas in Figure 11 and Figure 12. Outside of these altitudes (i.e. below 56 km and above 90 km) the MR weakens and the OH values in these regions should be interpreted with caution as the information from the a priori becomes important. The AVK FWHM values shown in Figure 12b indicate altitude resolutions decreasing from 10.2 km in the lower mesosphere to 16.6 km in the upper mesosphere, at altitudes below 90 km. Dividing the 10 retrieved altitude range (~34 km) by the DOFS over the same range (~3.0) gives an estimated altitude resolution of 11.0 km, similar to that obtained from the AVK FWHM values. The observation errors ( $\sigma_{obs}$ ) shown in Figure 12c have typical values of 2.1 ppbv and are smaller outside of the range of the AVK peaks as the retrieval tends to the a priori values in these regions and the contribution from the measurement is small. The total retrieval errors ( $\sigma_{tot}$ ) shown in Figure 12d are in the range 7.1–9.0 ppbv, and outside the range of AVK peaks tend towards the larger a priori standard deviations.

15 The results of the MC error analysis using retrievals from 500 simulated spectra in which OH and H<sub>2</sub>O profiles were randomly scaled by 0.5–2.0 are shown in Figure 12e–f. Over the trustable altitude range the mean difference ( $\mu_{MC}$ ) between the MC retrieved and “true” profiles is in the range -1.4–1.6 ppbv. The standard deviation ( $\sigma_{MC}$ ) of the individual retrievals is an estimator for the uncertainty of the OH retrieval, and the mean value of 2.6 ppbv is similar the mean observation error determined from single retrievals ( $\sigma_{obs}$ ). Both parameters depend on the signal-to-noise ratio of the input spectrum but  $\sigma_{MC}$  20 may more realistically represent actual observations where mesospheric OH profiles and column H<sub>2</sub>O show large variability. The Jacobian and gain matrices of the OH vertical polarisation forward model indicate that, as for O<sub>3</sub>, the OH emission line should be adequately sampled by an instrument with 10 kHz frequency resolution for all altitudes where the OH measurement contributes significantly to the retrieval. The values of the Jacobian, normalised by the layer thickness of the retrieval grid for observations at an 82° zenith angle, are shown in Figure 13. Typical values of the Jacobian are ~0.09 mK (ppbv)<sup>-1</sup>km<sup>-1</sup> at 25 mesospheric altitudes of 60–90 km where sub-storms are predicted to have the largest effect on OH abundance. The predicted changes in OH VMR, by up to ~20 ppbv for the altitude range 64–84 km, will have a small effect on the measured atmospheric brightness temperatures, producing a ~10 mK increase close to the emission line centre. However, the enhanced OH microwave signal during sub-storm activity would be measurable with a baseline noise of 1 mK for a 6-hour integration.

#### 4 Conclusions

30 The proof-of-concept simulations demonstrate that changes in O<sub>3</sub> and OH abundance in the high-latitude / polar middle and upper atmosphere, associated with geomagnetic sub-storm and other EEP processes, could be profiled using ground-based passive microwave measurements in the Ku-band 11–14 GHz region and OEM retrieval. At these frequencies tropospheric

attenuation is small and mesospheric emission signals are transmitted to the ground with low loss. Comparable, high atmospheric transmittances are calculated for various high-latitude NH and Antarctic sites in winter and summer, suggesting that different meteorology and location should have little impact on the proposed O<sub>3</sub> and OH observations.

For a radiometer performing 6 h measurements of the 11.072 GHz O<sub>3</sub> emission line with 10 kHz frequency resolution and a rms baseline noise of 1 mK, O<sub>3</sub> could be profiled over  $8 \times 10^{-4}$ –0.22 hPa (~98–58 km) with 11–18 km height resolution (~12 km from DOFS analysis) and ~1 ppmv uncertainty. For the equivalent OH 13.441 GHz measurement, demonstrated for vertical sensor polarisation, OH could be profiled over  $3 \times 10^{-3}$ –0.29 hPa (~90–56 km), also with 10–17 km height resolution (~11 km from DOFS analysis) and ~3 ppbv uncertainty. Such observations would allow the diurnal variations in mesospheric O<sub>3</sub> and OH to be characterised when abundances are relatively high, e.g. during night-time and polar winter. Measurement times of 24 h or longer would be necessary with less sensitive receivers or for measuring lower abundances. However, these measurements would still provide valuable data, in particular for the secondary ozone layer above 90 km as satellite measurements of this region become increasingly sparse. We have used simulations of atmospheric spectra from Kilpisjärvi, Finland as a test case to assess the feasibility of such measurements but demonstrate that similar results would be achieved by instruments deployed at other high-latitude NH sites and in Antarctica.

LNB receivers operating at the Ku-band emission frequencies of O<sub>3</sub> and OH are commercially available. LNBS covering the O<sub>3</sub> frequency (11.072 GHz) have noise factor typically in the range 0.7–1.3 dB, although suppliers specify values as low as 0.1 dB. For coverage of the OH emission line frequency (13.441 GHz) the stated LNB noise factor is ~1.2 dB. However, measurements reported by Tenneti and Rogers (2009) suggest that inexpensive satellite TV downconverters can achieve a noise factor as low as ~0.23 dB. If this high level of LNB performance is confirmed, a single receiver operating at room temperature would achieve 6 h O<sub>3</sub> spectrum measurements with the required rms baseline noise level of 1 mK. Otherwise, for the proposed O<sub>3</sub> and OH observations, either simultaneous measurements by an array of multiple receivers or using single receivers cooled to ~168 K for O<sub>3</sub> and ~46 K for OH would be needed. Monitoring of O<sub>3</sub> in the same volume of the atmosphere using three LNB receivers mounted in front of a “Direct TV” offset parabolic dish has been reported (Rogers et al., 2012). With six spectrometers simultaneously measuring both polarisations from each of the three receivers, in the ideal case the improvement in signal-to-noise compared to a single radiometer is  $\sqrt{6} = \sim 2.4$ , although non-optimum matching of the LNB beam profiles and antenna focus would impact on the performance. Scaling up to 24 independent spectrometers for the O<sub>3</sub> measurements would be relatively straightforward using 12 receivers each measuring both polarisations, mounted singly or with two or three LNBS bundled together at each antenna focus point. Atmospheric observations recorded by each spectrometer could then be combined to achieve a  $\sqrt{24} = \sim 4.9$  improvement in signal-to-noise. For OH, the greater complexity and cost of constructing 80 independent spectrometers operating at 13.441 GHz could make use of a single low temperature receiver the better option. For low temperature operation, liquid nitrogen-cooled cryostats readily attain ~90 K, meeting the requirements for O<sub>3</sub> observations. However, this cooling method requires a supply of liquid nitrogen into either a continuous flow or reservoir design of cryostat. Alternatively, LNBS mounted on the cold-head of a Gifford-McMahon closed-cycle

helium cryocooler (e.g., Radebaugh, 2009; de Waele, 2011) could be operated continuously at temperatures in the range 4–77 K.

The next steps towards developing suitable instruments include selecting and testing commercially-available LNB receiver and antenna components and verifying the optimum configuration for making the proposed mesospheric O<sub>3</sub> and OH observations. If tests confirm that low-cost satellite TV components can reliably achieve the desired performance (e.g., LNBs with noise factor of 0.23 dB or lower) then the increased complexity and cost of designing and building a system using numerous multiple receivers or cryogenic cooling would be avoided, for O<sub>3</sub> 11.072 GHz measurements at least. It should be noted that other natural and man-made sources may produce signals at frequencies that overlap the O<sub>3</sub> and OH microwave emissions. Potential interference from such sources may be mitigated by observing at remote, high-latitude locations and by carefully pointing the receiver antenna to minimise directional pick-up of spurious signals in the instrument field-of-view. OH microwave line Zeeman splitting needs to be adequately modelled in the retrieval algorithm, and the spectroscopic parameters need to be verified and optimised. Furthermore, during geomagnetic storms rapid, localised fluctuations in the Earth's magnetic field can occur which may not be well reproduced by a priori data from models such as IGRF. Instead, a better approach may be to use magnetometer data provided by nearby geophysical observatories to constrain the OH retrievals, or to allow the retrieval to adjust the magnetic field from a priori values to give an optimum fit to the observed line-shape.

## 5 Data availability

The model and simulation datasets (Newnham et al., 2018) used in this study are available from the UK Polar Data Centre (<https://www.bas.ac.uk/data/uk-pdc/>).

*Acknowledgements.* This work has been supported in part by the UK's Natural Environment Research Council (NERC) Technologies Proof-of-Concept grant reference NE/P003478/1 “Satellite TV-based Ozone and OH Observations using Radiometric Measurements (STO<sub>3</sub>RM)” awarded to DAN. The work of P. T. Verronen was supported by the Academy of Finland (project 276926 - SECTIC: Sun-Earth Connection Through Ion Chemistry). The authors thank the ARTS and Qpack development teams and P. Kirsch at BAS for assistance configuring and running the code, M. E. Andersson (FMI) for providing WACCM-D datasets, and A. E. E. Rogers at the Massachusetts Institute of Technology (MIT) Haystack Observatory for helpful discussions. Aaron Hendry is acknowledged for providing computer code (GEO2CGM) to facilitate the conversion from spherical geographic coordinates to spherical corrected geomagnetic coordinates.

## References

- Andersson, M. E., Verronen, P. T., Rodger, C. J., Clilverd, M. A., and Seppälä, A.: Missing driver in the Sun–Earth connection from energetic electron precipitation impacts mesospheric ozone, *Nature Comms.*, 5, 5197, doi:10.1038/ncomms6197, 2014a.
- 5 Andersson, M. E., Verronen, P. T., Rodger, C. J., Clilverd, M. A., and Wang, S.: Longitudinal hotspots in the mesospheric OH variations due to energetic electron precipitation, *Atmos. Chem. Phys.*, 14, 1095–1105, <https://doi.org/10.5194/acp-14-1095-2014>, 2014b.
- Arsenovic, P., Rozanov, E., Stenke, A., Funke, B., Wissing, J. M., Mursula, K., Tummon, F., and Peter, T., The influence of middle range energy electrons on atmospheric chemistry and regional climate, *J. Atmos. Sol.-Terr. Phys.*, 149, 180–190, doi:10.1016/j.jastp.2016.04.008, 2016.
- 10 Baumgaertner, A. J. G., Seppälä, A., Jöckel, P., and Clilverd, M. A.: Geomagnetic activity related NO<sub>x</sub> enhancements and polar surface air temperature variability in a chemistry climate model: Modulation of the NAM index, *Atmos. Chem. Phys.*, 11(9), 4521–4531, doi:10.5194/acp-11-4521-2011, 2011.
- Brasseur, G. P., and Solomon, S.: *Aeronomy of the Middle Atmosphere*, 3rd ed., Springer, Dordrecht, Netherlands, 2005.
- 15 Brinksma, E. J., Meijer, Y. J., McDermid, I. S., Cageao, R. P., Bergwerff, J. B., Swart, D. P. J., Ubachs, W., Matthews, W. A., Hogervorst, W., and Hovenier J. W.: First lidar observations of mesospheric hydroxyl, *Geophys. Res. Lett.*, 25(1), 51–54, doi:10.1029/97GL53561, 1998. (Erratum, *Geophys. Res. Lett.*, 25, 521, 1998.)
- Buehler, S. A., Eriksson, P., Kuhn, T., von Engel, A., and Verdes, C.: ARTS, the atmospheric radiative transfer simulator, *J. Quant. Spectrosc. Radiat. Transfer*, 91(1), 65–93, doi:10.1016/j.jqsrt.2004.05.051, 2005.
- 20 Buehler, S. A., Mendrok, J., Eriksson, P., Perrin, A., Larsson, R., and Lemke, O.: ARTS, the Atmospheric Radiative Transfer Simulator – version 2.2, the planetary toolbox edition, *Geosci. Model Dev.*, 11, 1537–1556, doi:10.5194/gmd-11-1537-2018, 2018.
- Christensen, O. M., and Eriksson, P.: Time series inversion of spectra from ground-based radiometers, *Atmos. Meas. Tech.*, 6, 1597–1609, doi:10.5194/amt-6-1597-2013, 2013.
- 25 Clancy, R. T., Sandor, B. J., Rusch, D. W., and Muhleman, D. O.: Microwave observations and modeling of O<sub>3</sub>, H<sub>2</sub>O, and HO<sub>2</sub> in the mesosphere, *J. Geophys. Res.*, 99(D3), 5465–5473, doi:10.1029/93JD03471, 1994.
- Clough, S., Shephard, M., Mlawer, E., Delamere, J., Iacono, M., Cady-Pereira, K., Boukabara, S., and Brown, P.: Atmospheric radiative transfer modeling: a summary of the AER codes, *J. Quant. Spectrosc. Ra.*, 91, 233–244, 2005.
- Cresswell-Moorcock, K., Rodger, C. J., Kero, A., Collier, A. B., Clilverd, M. A., Häggström, I., and Pitkänen, T.: A reexamination of latitudinal limits of substorm-produced energetic electron precipitation, *J. Geophys. Res. - Space Phys.*, 30 118, 6694–6705, doi:10.1002/jgra.50598, 2013.
- de Waele, A. T. A. M.: Basic operation of cryocoolers and related thermal machines, *J. Low Temp. Phys.*, 164, 179, [doi:10.1007/s10909-011-0373-x](https://doi.org/10.1007/s10909-011-0373-x), 2011.

- Englert, C. R., Stevens, M. H., Siskind, D. E., Harlander, J. M., and Roesler, F. L.: Spatial Heterodyne Imager for Mesospheric Radicals on STPSat-1, *J. Geophys. Res.*, 115, D20306, doi:10.1029/2010JD014398, 2010.
- Eriksson, P., Jiménez, C., and Buehler, S. A.: Qpack, a general tool for instrument simulation and retrieval work, *J. Quant. Spectrosc. Radiat. Transfer*, 91(1), 47–64, doi:10.1016/j.jqsrt.2004.05.050, 2005.
- 5 Eriksson, P., Buehler, S. A., Davis, C. P., Emde, C., and Lemke, O.: ARTS, the atmospheric radiative transfer simulator, version 2, *J. Quant. Spectrosc. Radiat. Transfer*, 112(10), 1551–1558, doi:10.1016/j.jqsrt.2011.03.001, 2011.
- Finlay, C. C., et al.: International geomagnetic reference field: The eleventh generation, *Geophys. J. Int.*, 183(3), 1216–1230, doi:10.1111/j.1365-246X.2010.04804.x, 2010.
- Froidevaux, L., et al.: Validation of Aura Microwave Limb Sounder stratospheric ozone measurements, *J. Geophys. Res.*, 113, D15S20, doi:10.1029/2007JD008771, 2008.
- 10 Gordon, I. E., et al.: The HITRAN2016 molecular spectroscopic database, *J. Quant. Spectrosc. Radiat. Transfer*, 203, 3–69, doi:10.1016/j.jqsrt.2017.06.038, 2017.
- Hartogh, P., Jarchow, C., Sonnemann G. R., and Grygalashvyly, M.: On the spatiotemporal behavior of ozone within the mesosphere/mesopause region during nearly polar night conditions, *J. Geophys. Res.*, 109, D18303, doi:10.1029/2004JD004576, 2004.
- 15 Jackman, C. H., and McPeters, R. D.: The effect of solar proton events on ozone and other constituents, *Solar variability and its effects on climate*, Geophysical Monograph Series (Vol. 141, pp. 305–319), Washington, DC: American Geophysical Union, doi:10.1029/141GM21, 2004.
- Kraus, J. D.: *Radio astronomy*, Powell, Ohio, Cygnus-Quasar, 2nd edition, ISBN-10:1882484002, ISBN-13:9781882484003, June 1986.
- 20 Kuntz, M.: A new implementation of the Humlicek algorithm for the calculation of the Voigt profile function, *J. Quant. Spectrosc. Ra.*, 57, 819–824, 1997.
- Larsson, R., Buehler, S. A., Eriksson P., and Mendrok, J.: A treatment of the Zeeman effect using Stokes formalism and its implementation in the Atmospheric Radiative Transfer Simulator (ARTS), *J. Quant. Spectrosc. Radiat. Transfer*, 133, 445–453, doi:10.1016/j.jqsrt.2013.09.006, 2014.
- 25 Marsh, D. R., Mills, M. J., Kinnison, D. E., and Lamarque, J. -F.: Climate change from 1850 to 2005 simulated in CESM1 (WACCM), *J. Climate*, 26, 7372–7391, doi:10.1175/JCLI-D-12-00558.1, 2013.
- Melsheimer, C., et al.: Intercomparison of general purpose clear sky atmospheric radiative transfer models for the millimeter/submillimeter spectral range, *Radio Sci.*, 40, RS1007, doi:10.1029/2004RS003110, 2005.
- 30 Minschwaner, K., Manney, G. L., Wang, S. H., and Harwood, R. S.: Hydroxyl in the stratosphere and mesosphere – Part 1: Diurnal variability, *Atmos. Chem. Phys.*, 11, 955–962, doi:10.5194/acp-11-955-2011, 2011.
- Mironova, I. A., Aplin, K. L., Arnold, F., Bazilevskaya, G. A., Harrison, R. G., Krivolutsky, A. A., et al.: Energetic particle influence on the Earth’s atmosphere, *Space Science Reviews*, 194, 1–96, doi:10.1007/s11214-015-0185-4, 2015.

- Mlawer, E. J., Payne, V. H., Moncet, J. -L., Delamere, J. S., Alvarado, M. J., and Tobin, D. C.: Development and recent evaluation of the MT-CKD model of continuum absorption, *Philos. T. R. Soc. A*, 370, 2520–2556, 2012.
- Newnham, D. A., et al.: Observations and modeling of increased nitric oxide in the Antarctic polar middle atmosphere associated with geomagnetic storm-driven energetic electron precipitation, *J. Geophys. Res. - Space Phys.*, 123, doi:10.1029/2018JA025507, 2018.
- 5 Newnham, D., Verronen, P., and Seppälä, A.: Model data for simulating atmospheric microwave spectra at 11.072 GHz and 13.441 GHz and performing retrievals of ozone (O<sub>3</sub>) and hydroxyl (OH) vertical profiles, Polar Data Centre, Natural Environment Research Council, UK, doi:10.5285/57858a9a-d814-412c-8e79-9a542cd055d4, 2018.
- Pickett, H. M., et al.: Validation of Aura Microwave Limb Sounder OH and HO<sub>2</sub> measurements, *J. Geophys. Res.*, 113, D16S30, doi:10.1029/2007JD008775, 2008.
- 10 Radebaugh, R.: Cryocoolers: the state of the art and recent developments, *J. Phys.: Condensed Matter*, 21, 164219, doi:10.1088/0953-8984/21/16/164219, 2009.
- Radford, H. E.: Microwave Zeeman effect of free hydroxyl radicals, *Phys. Rev.* 122, 114, doi:10.1103/PhysRev.122.114, 1961.
- 15 Rodger, C. J., Cresswell-Moorcock, K., and Clilverd, M. A.: Nature’s Grand Experiment: Linkage between magnetospheric convection and the radiation belts, *J. Geophys. Res. Space Physics*, 121, 171–189, doi: 10.1002/2015JA021537, 2016.
- Rodgers, C. D.: *Inverse methods for atmospheric sounding: Theory and Practice*, vol. 2 of Series on Atmospheric, Ocean and Planetary Physics, World Scientific, doi:10.1142/3171, 2000.
- Rogers, A. E. E., Lekberg, M., and Pratap, P.: Seasonal and diurnal variations of ozone near the mesopause from observations of the 11.072-GHz line, *J. Atmos. Oceanic Technol.*, 26, 2192–2199, doi:10.1175/2009JTECHA1291.1, 2009.
- 20 Rogers, A. E. E., Erickson, P., Fish, V. L., Kittredge, J., Danford, S., Marr, J. M., Arndt, M. B., Sarabia, J., Costa, D., and May, S. K.: Repeatability of the seasonal variations of ozone near the mesopause from observations of the 11.072-GHz line, *J. Atmos. Oceanic Technol.*, 29, 1492–1504, doi:10.1175/JTECH-D-11-00193.1, 2012.
- Ryan, N. J., Walker, K. A., Raffalski, U., Kivi, R., Gross, J., and Manney, G. L.: Ozone profiles above Kiruna from two ground-based radiometers, *Atmos. Meas. Tech.*, 9, 4503–4519, doi:10.5194/amt-9-4503-2016, 2016.
- 25 Sastry, K. V. L. N., and Vanderlinde, J.: Low-field Zeeman effect of OH in the <sup>2</sup>Π<sub>3/2</sub>, J = 7/2, 9/2, 11/2, 13/2, and 15/2 states, *J. Mol. Spectrosc.*, 83(2), 332–338, doi:10.1016/0022-2852(80)90057-0, 1980.
- Semeniuk, K., Fomichev, V. I., McConnell, J. C., Fu, C., Melo, S. M. L., and Usoskin, I. G.: Middle atmosphere response to the solar cycle in irradiance and ionizing particle precipitation, *Atmos. Chem. Phys.*, 11(10), 5045–5077, doi:10.5194/acp-11-5045-2011, 2011.
- 30 Seppälä, A., Randall, C. E., Clilverd, M. A., Rozanov, E., and Rodger, C. J.: Geomagnetic activity and polar surface air temperature variability, *J. Geophys. Res. Space Phys.*, 114, A10312, doi:10.1029/2008JA014029, 2009.
- Seppälä, A., Lu, H., Clilverd, M. A., and Rodger, C. J.: Geomagnetic activity signatures in wintertime stratosphere wind, temperature, and wave response, *J. Geophys. Res. Atmos.*, 118, 2169–2183, doi:10.1002/jgrd.50236, 2013.

- Seppälä, A., Clilverd, M. A., Beharrell, M. J., Rodger, C. J., Verronen, P. T., Andersson, M. E., and Newnham, D. A.: Substorm-induced energetic electron precipitation: Impact on atmospheric chemistry, *Geophys. Res. Lett.*, 42, 8172–8176, doi:10.1002/2015GL065523, 2015.
- Sinnhuber, M., Nieder, H., and Wieters, N.: Energetic particle precipitation and the chemistry of the mesosphere/lower  
5 thermosphere: *Surv. Geophys.*, 33, 1281–1334, doi:10.1007/s10712-012-9201-3, 2012.
- Siskind, D. E., Stevens, M. H., Englert, C. R., and Mlynczak, M. G.: Comparison of a photochemical model with observations of mesospheric hydroxyl and ozone, *J. Geophys. Res.*, 118, 195–207, doi:10.1029/2012JD017971, 2013.
- Smith, A. K., et al.: Satellite observations of ozone in the upper mesosphere, *J. Geophys. Res. Atmos.*, 118, 5803–5821, doi:10.1002/jgrd.50445, 2013.
- 10 Smith, S. M., Baumgardner, J., Mertens, C. J., Russell, J. M., Mlynczak, M. G., and Mendillo, M.: Mesospheric OH temperatures: Simultaneous ground-based and SABER OH measurements over Millstone Hill, *Adv. Space Res.*, 45, 239–246, doi:10.1016/j.asr.2009.09.022, 2010.
- Summers, M. E., Conway, R. R., Siskind, D. E., Stevens, M. H., Offermann, D., Riese, M., Preusse, P., Strobel, D. F., and  
15 Russell III, J. M.: Implications of satellite OH observations for middle atmospheric H<sub>2</sub>O and ozone, *Science*, 277, 1967–1969, 1997.
- Tenneti, S. N., and Rogers, A. E. E.: Development of an optimized antenna and other enhancements of a spectrometer for the study of ozone in the mesosphere, VSRT and MOSAIC Memo 063 (2009).Thébault, E., et al.: International Geomagnetic Reference Field: the 12th generation, *Earth, Planets and Space*, 67, 79, doi:10.1186/s40623-015-0228-9, 2015.
- Turunen, E., Verronen, P. T., Seppälä, A., Rodger, C. J., Clilverd, M. A., Tamminen, J., Enell, C.-F., and Ulich, T.: Impact of  
20 different energies of precipitating particles on NO<sub>x</sub> generation in the middle and upper atmosphere during geomagnetic storms, *J. Atmos. Sol. Terr. Phys.*, 71(10–11), 1176–1189, doi:10.1016/j.jastp.2008.07.005, 2009.
- Van Vleck, J., and Huber, D.: Absorption, emission, and line-breadths: A semi-historical perspective, *Rev. Mod. Phys.*, 49, 939, doi:10.1103/RevModPhys.49.939, 1977.
- Verronen, P. T., Seppälä, A., Clilverd, M. A., Rodger, C. J., Kyrölä, E., Enell, C. -F., Ulich, T., and Turunen, E.: Diurnal  
25 variation of ozone depletion during the October–November 2003 solar proton events, *J. Geophys. Res.*, 110, A09S32, doi:10.1029/2004JA010932, 2005.
- Verronen, P. T., Rodger, C. J., Clilverd, M. A., and Wang, S.: First evidence of mesospheric hydroxyl response to electron precipitation from the radiation belts, *J. Geophys. Res.*, 116, D07307, doi:10.1029/2010JD014965, 2011.
- Verronen, P.T., and Lehmann, R.: Analysis and parameterisation of ionic reactions affecting middle atmospheric HO<sub>x</sub> and NO<sub>y</sub>  
30 during solar proton events, *Ann. Geophys.*, 31, 909–956, doi:10.5194/angeo-31-909-2013, 2013.
- Verronen, P. T., and Lehmann, R.: Enhancement of odd nitrogen modifies mesospheric ozone chemistry during polar winter, *Geophys. Res. Lett.*, 42, doi:10.1002/2015GL066703, 2015.
- Verronen, P. T., Andersson, M. E., Marsh, D. R., Kovács, T., and Plane, J. M. C.: WACCM-D—Whole Atmosphere Community Climate Model with D-region ion chemistry, *J. Adv. Model. Earth Syst.*, 8, doi:10.1002/2015MS000592, 2016.

- von Zahn, U., Fricke, K. H., Gerndt, R., and Blix, T.: Mesospheric temperatures and the OH layer height as derived from ground-based lidar and OH\* spectrometry, *J. Atmos. Terr. Phys.*, 49, 863–869, doi:10.1016/0021-9169(87)90025-0, 1987.
- Yee, J.-H., Crowley, G., Roble, R. G., Skinner, W. R., Burrage, M. D., and Hays, P. B.: Global simulations and observations of O(<sup>1</sup>S), O<sub>2</sub>(<sup>1</sup>Σ) and OH mesospheric nightglow emissions, *J. Geophys. Res.*, 102(A9), 19949–19968, doi:10.1029/96JA01833, 1997.
- 5 Zhang, S. P., and Shepherd, G. S.: The influence of the diurnal tide on the O(<sup>1</sup>S) and OH emission rates observed by WINDII on UARS, *Geophys. Res. Lett.*, 26, 529–532, doi:10.1029/1999GL900033, 1999.
- Zawedde, A. E., NesseTyssøy, H., Stadsnes, J., and Sandanger, M. I.: The impact of energetic particle precipitation on mesospheric OH - Variability of the sources and the background atmosphere, *J. Geophys. Res. Space Physics*, 123, doi:10.1029/2017JA025038, 2018.

**Table 1.** Calculated performance for ozone (O<sub>3</sub>) 11.072 GHz and hydroxyl (OH) 13.441 GHz radiometers with 10 kHz frequency resolution.

	O <sub>3</sub> 11.072 GHz				OH 13.441 GHz		
Noise factor (dB)	1.3	0.7	0.7	0.7	1.2	1.2	1.2
Reference temperature (K)	290	290	290	168	290	290	46
System noise temperature (K)	101	51	51	15	92	92	15
Number of measurement channels	2	2	24	2	2	80	2
Measurement time (h)	24	24	6	6	24	6	6
1 $\sigma$ rms noise (K)	3.4	1.7	1.0	1.0	3.1	1.0	1.0

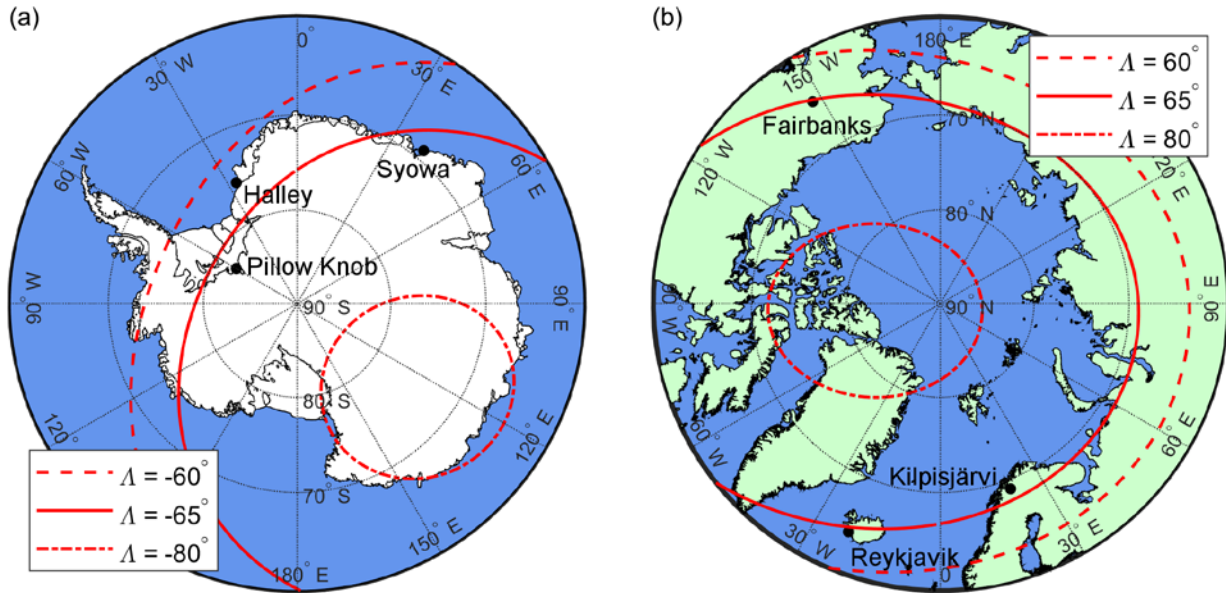


**Figure 1:** Maps of a) the southern hemisphere and Antarctica poleward of geographic latitude 60°S and b) the northern hemisphere and Arctic region poleward of geographic latitude 60°N. The red dashed, solid and dot-dashed lines on each map show the geomagnetic latitudes  $\Lambda = \pm 60^\circ$ ,  $\Lambda = \pm 65^\circ$ , and  $\Lambda = \pm 80^\circ$  respectively, calculated for 1 January 2015 and an altitude of 80 km using the IGRF-12 internal field model (Thébault et al., 2015). Filled black circles indicate the locations of Halley station (75°37'S, 26°15'W,  $\Lambda = -62.3^\circ$ ), Syowa station (69°00'S, 39°35'E,  $\Lambda = -66.6^\circ$ ), and Pillow Knob refuelling station (82°30'S, 60°00'W,  $\Lambda = -67.3^\circ$ ) in a) and Kilpisjärvi (69°03'N, 20°49'E,  $\Lambda = 66.2^\circ$ ), Finland, Reykjavik (64°08'N, 21°56'W,  $\Lambda = 64.4^\circ$ ), Iceland, and Fairbanks (64°51'N, 147°43'W,  $\Lambda = 65.2^\circ$ ), Alaska in b).

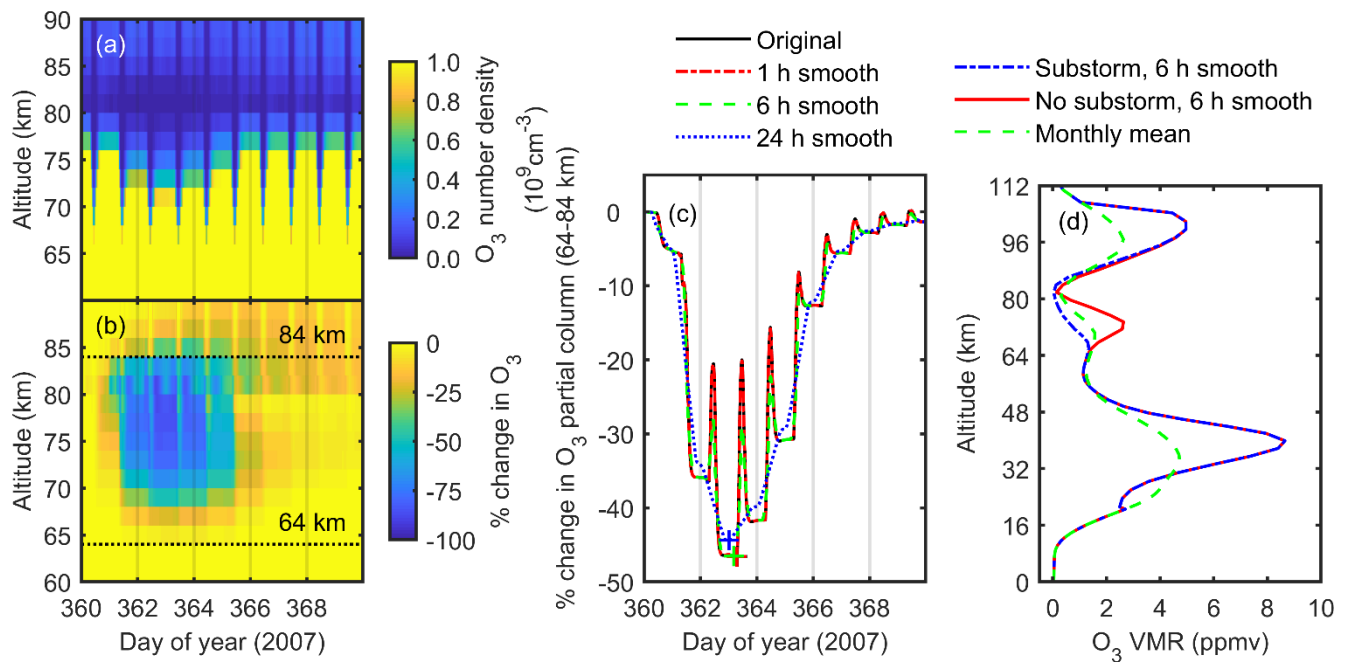
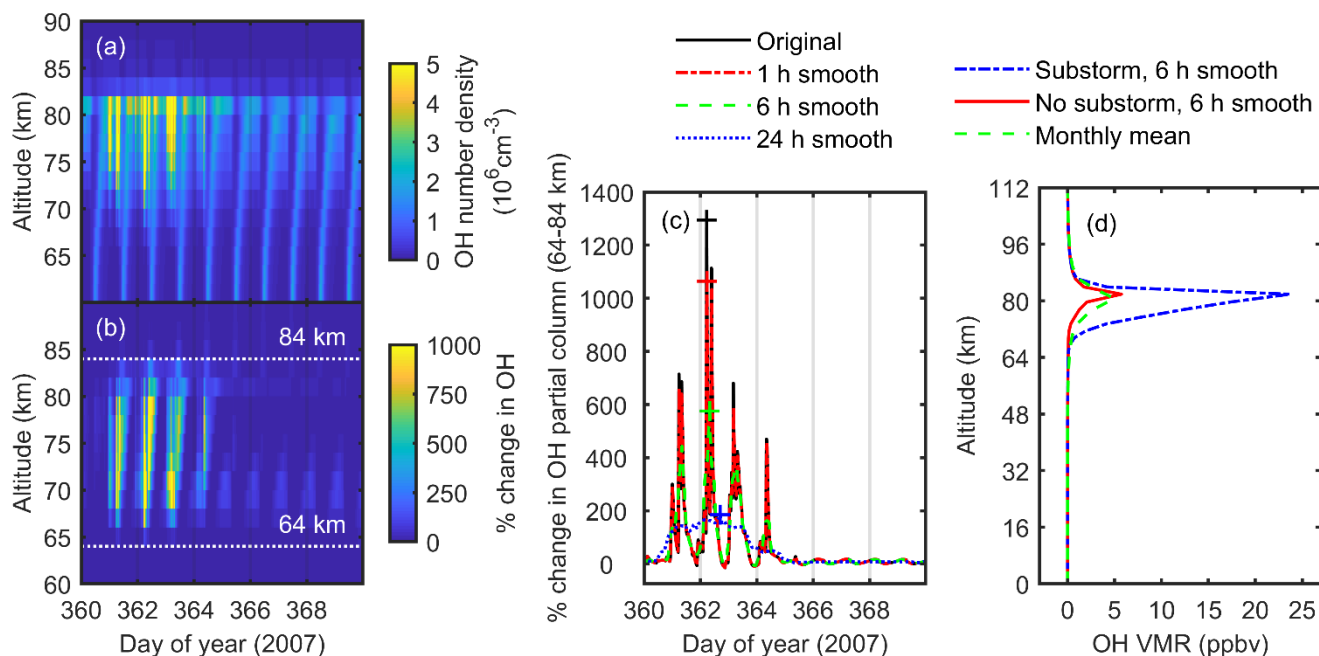


**Figure 2:** Derivation of ozone ( $\text{O}_3$ ) volume mixing ratio profiles from atmospheric model data-sets. Panel a) shows  $\text{O}_3$  number densities calculated by the SIC model for December 2007 sub-storm conditions at Kilpisjärvi ( $69^{\circ}03' \text{ N}$ ,  $20^{\circ}48' \text{ E}$ ), Finland. Panel b) shows the percentage change in modelled  $\text{O}_3$  abundance from background (no sub-storm) conditions. Panel c) shows the percentage change in  $\text{O}_3$  partial column over altitudes 64–84 km during sub-storm conditions for the original (15 min) model resolution and 1 h, 6 h, and 24 h smoothed data. ‘+’ symbols indicate the largest decreases in  $\text{O}_3$  partial column at each nominal time resolution. Plot d) shows the 6 h-smoothed  $\text{O}_3$  VMR profiles for December sub-storm, background (no sub-storm), and monthly mean conditions.



5 **Figure 3:** Derivation of hydroxyl radical (OH) volume mixing ratio profiles from atmospheric model data-sets. Panel a) shows OH number densities calculated by the SIC model for December 2007 sub-storm conditions at Kilpisjärvi (69°03' N, 20°48' E), Finland. Panel b) shows the percentage change in modelled O<sub>3</sub> abundance from background (no sub-storm) conditions. Panel c) shows the percentage change in OH partial column over altitudes 64–84 km during sub-storm conditions for the original (15 min) model resolution and 1 h, 6 h, and 24 h smoothed data. '+' symbols indicate the largest increases in OH partial column at each nominal time resolution. Plot d) shows the 6 h-smoothed OH VMR profiles for December sub-storm, background (no sub-storm), and monthly mean conditions.

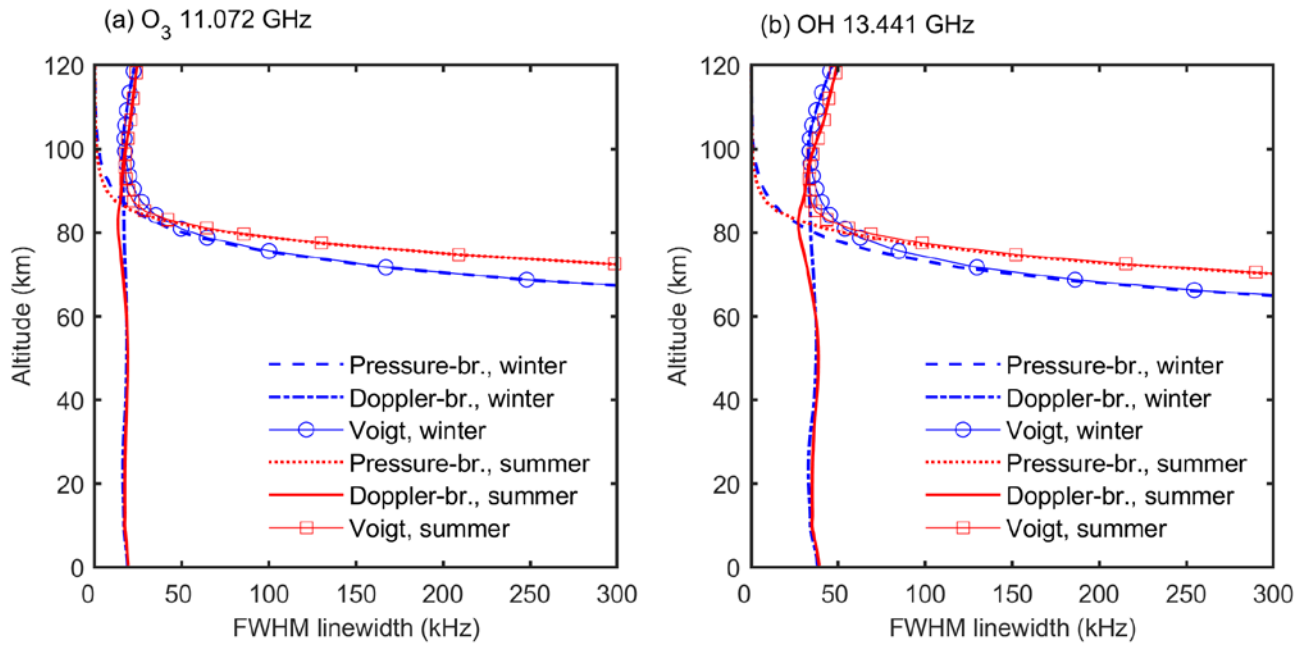


**Figure 4:** Pressure-broadened, Doppler-broadened, and Voigt full-width half-maxima (FWHM) linewidths for a) ozone (O<sub>3</sub>) 11.072 GHz and b) OH 13.441 GHz emission lines, calculated for mean winter (DJF) and mean summer (JJA) conditions at  
5 Kilpisjärvi (69°03' N, 20°48' E), Finland.

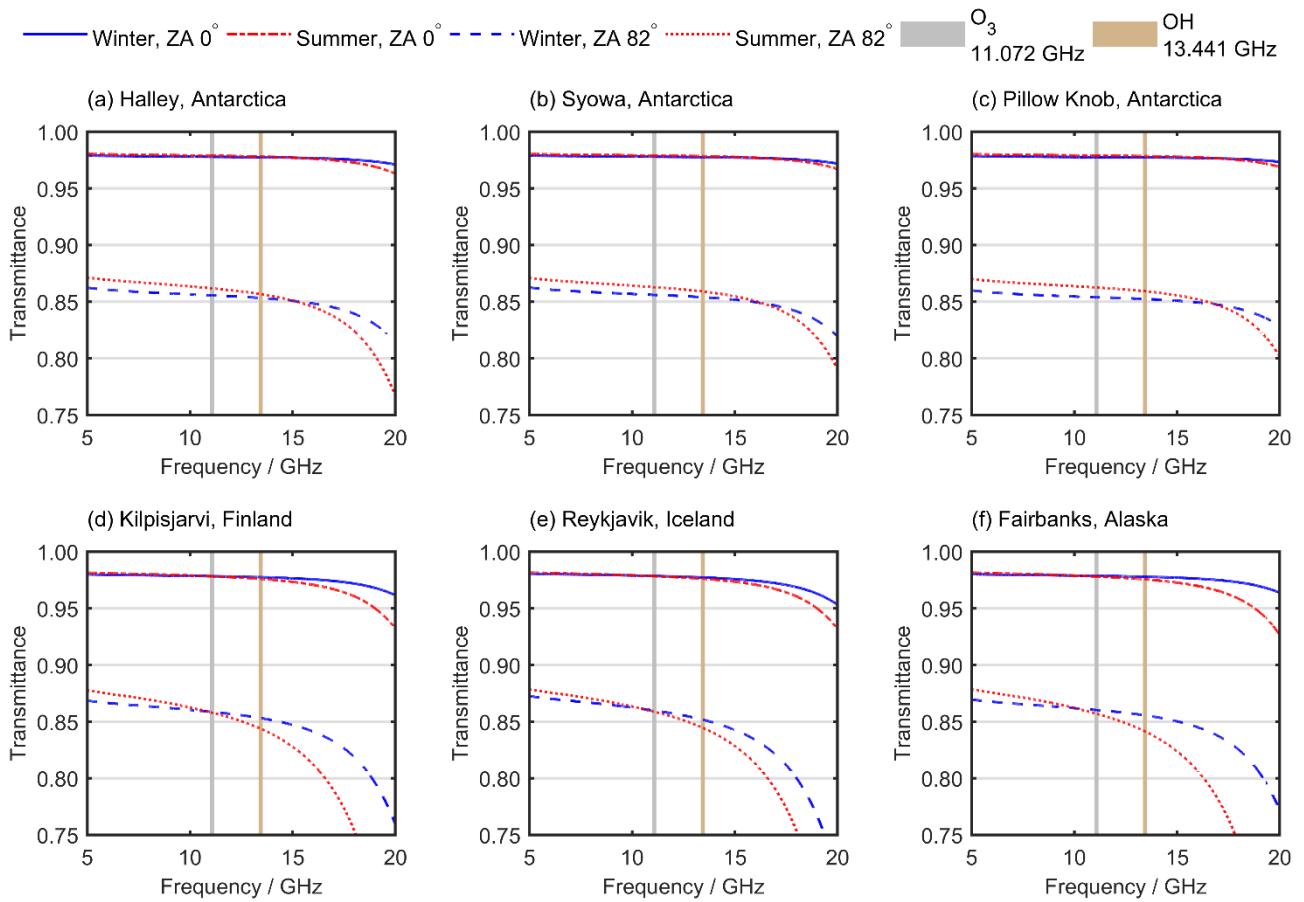
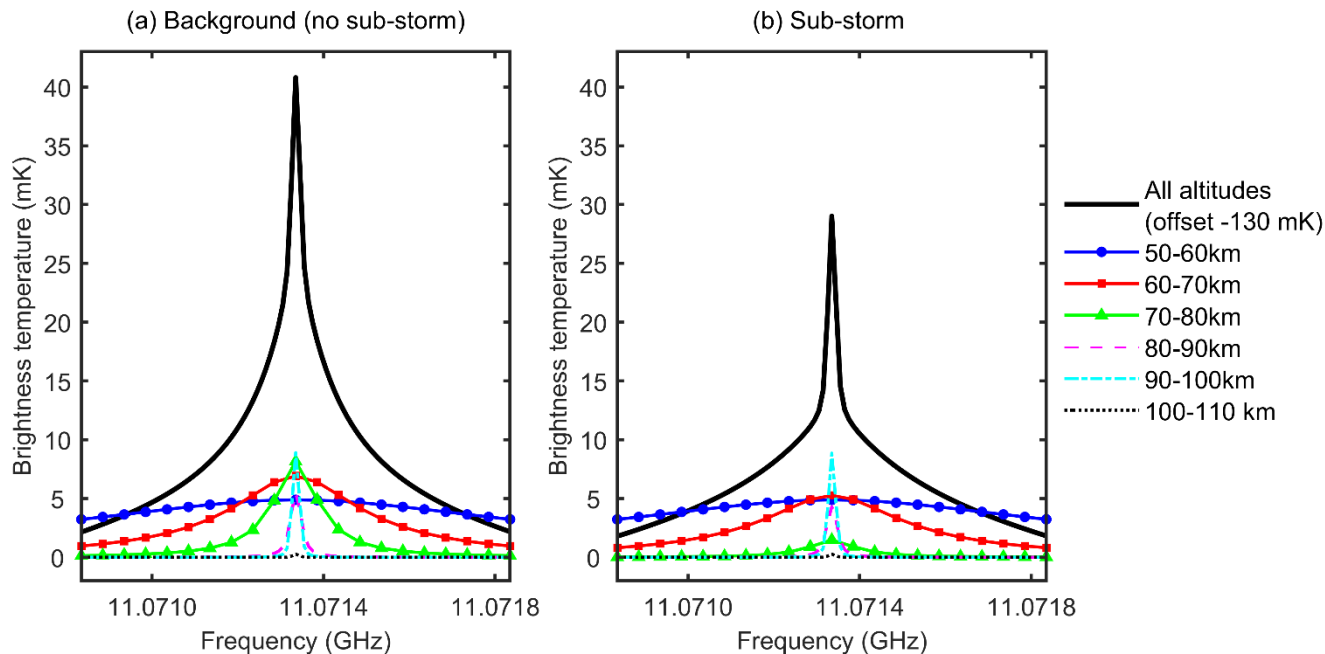


**Figure 5:** Survey atmospheric transmittance spectra at six polar locations for the frequency range 5–20 GHz, calculated on a 1 MHz frequency grid. In plots a)–c) transmittances calculated at zenith angle (ZA) 0° (i.e. viewing vertically upwards) and 82° are shown for mean summer (DJF) and mean winter (JJA) conditions at three Antarctic locations. In plots d)–f) transmittances calculated at ZA 0° and 82° are shown for mean summer (JJA) and mean winter (DJF) conditions at three Arctic locations. The light grey and light brown vertical lines indicate the frequencies of the ozone (O<sub>3</sub>, 11.072 GHz) and hydroxyl (OH, 13.441 GHz) emission lines.



5 **Figure 6:** Simulated atmospheric spectra for the ozone ( $O_3$ ) 11.072 GHz emission line in clear-sky, December conditions using a ground-based radiometer with 10 kHz frequency resolution,  $82^\circ$  zenith angle, and  $0^\circ$  azimuthal angle located at Kilpisjärvi ( $69^\circ 03' N$ ,  $20^\circ 48' E$ ), Finland. Solid black curves show the overall OH emission from all altitudes. Coloured lines show the contributions from 10 km altitude intervals in the range 50–110 km. Plots a) and b) show the spectra for background (no sub-storm) and sub-storm conditions respectively.

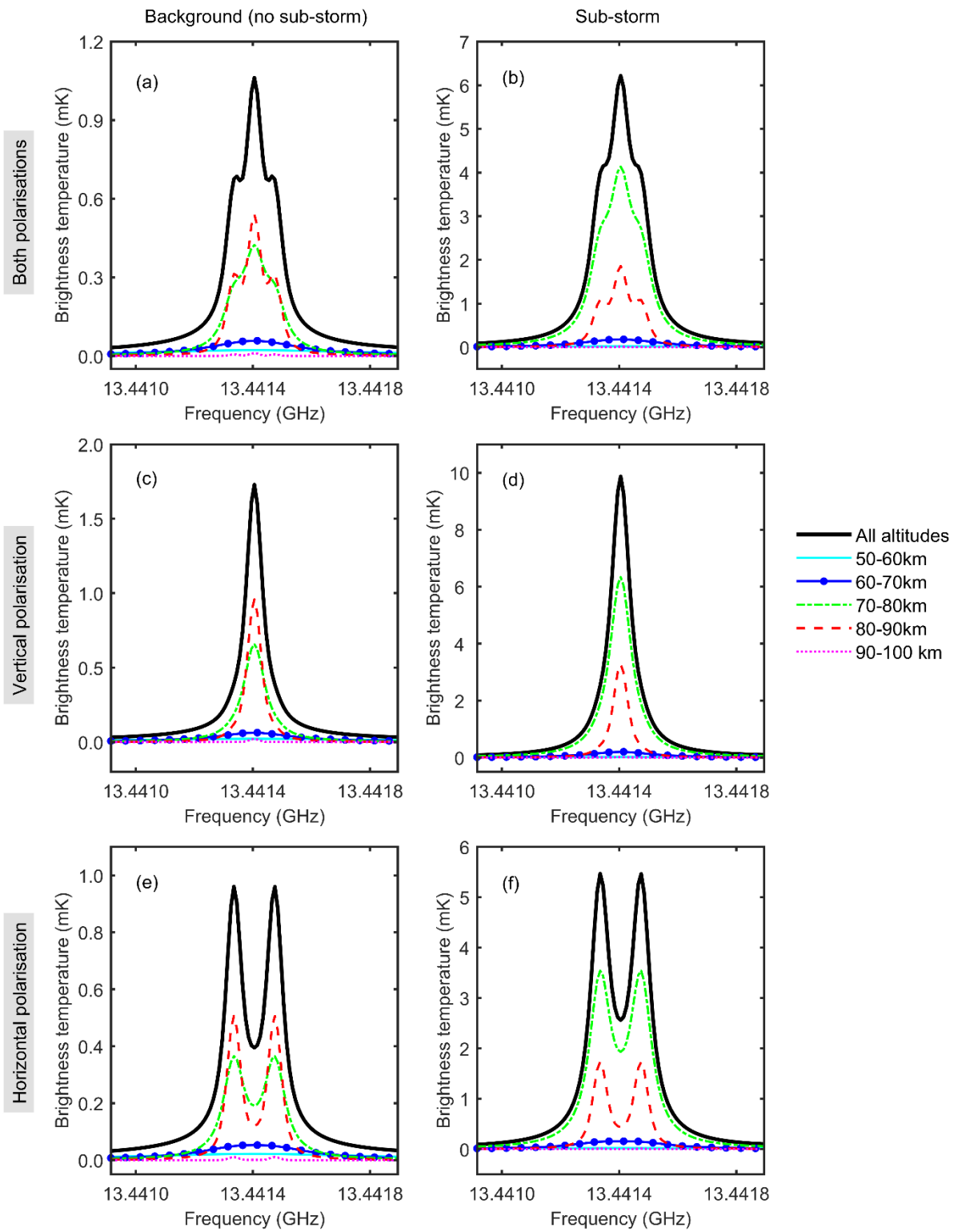


**Figure 7:** Simulated atmospheric spectra for the hydroxyl (OH) 13.441 GHz emission line in clear-sky, December conditions using a ground-based radiometer with 10 kHz frequency resolution, 82° zenith angle, and 0° azimuthal angle located at Kilpisjärvi (69°03' N, 20°48' E), Finland. Contributions from other atmospheric species have been removed to show changes in the brightness temperature spectra due to OH. Solid black curves show the overall OH emission from all altitudes. Coloured lines show the contributions from 10 km altitude intervals in the range 50–100 km. Plots a) and b) are for all sensor polarisations in background (no sub-storm) and sub-storm conditions respectively. Similarly, c) and d) are for vertical sensor polarisation and e) and f) are for horizontal sensor polarisation.

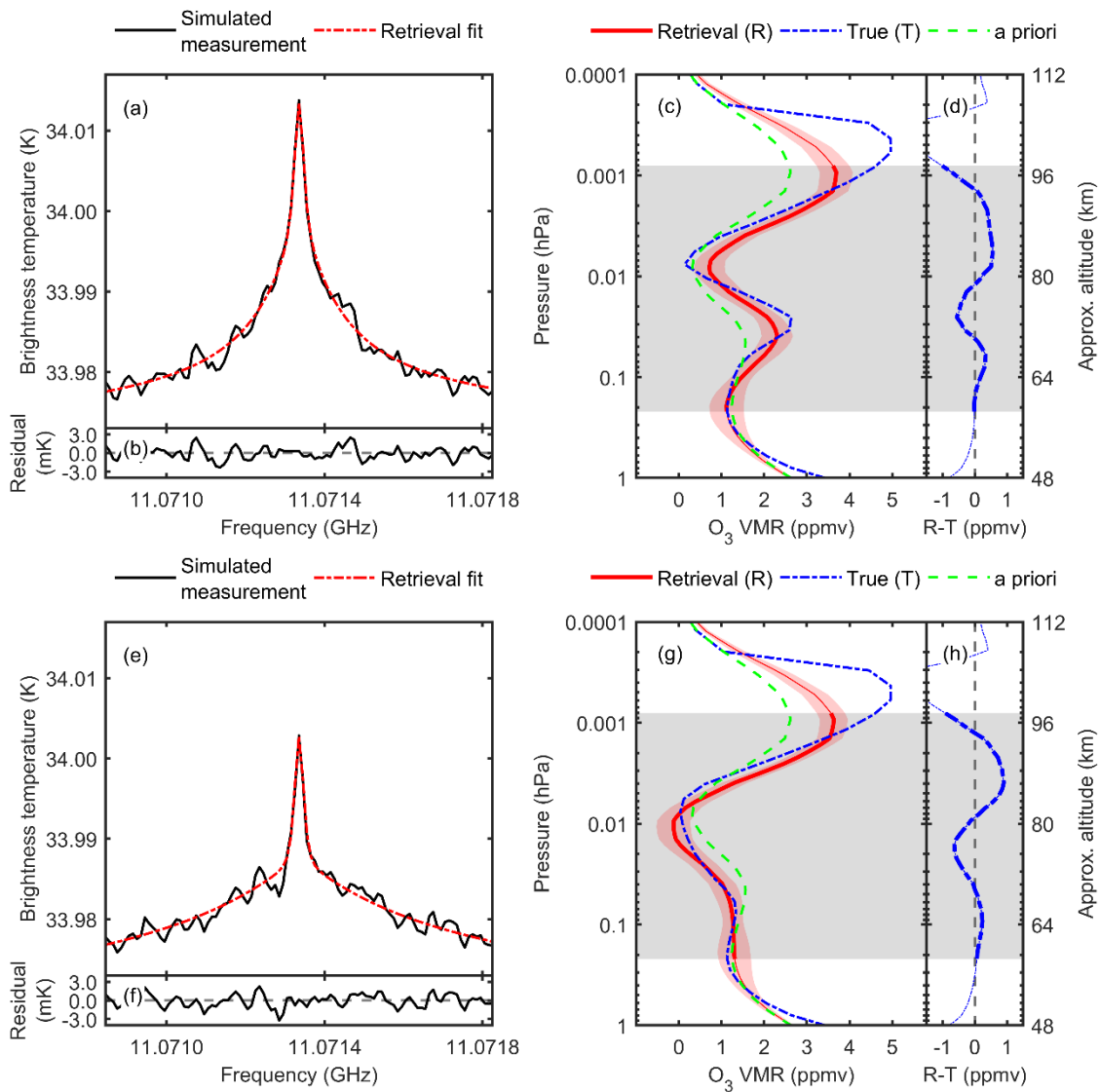


**Figure 8:** Ozone (O<sub>3</sub>) retrievals for simulated 6 h observations of the O<sub>3</sub> 11.072 GHz emission line in clear-sky December conditions using a ground-based radiometer at Kilpisjärvi (69°03' N, 20°48' E), Finland. The forward model clear-sky spectra are calculated using the model O<sub>3</sub> profiles for December 2007 with 1 mK baseline noise, 10 kHz frequency resolution, and 82° zenith angle. a)–d) show the results using background (no sub-storm) O<sub>3</sub> in the simulations, and e)–g) show the results for sub-storm O<sub>3</sub>. The simulated O<sub>3</sub> spectra and retrieval fits are shown in a) and e), and the residual differences in b) and f). The a priori, true, and retrieved O<sub>3</sub> volume mixing ratio profiles, and the differences between the retrieved and true profiles, are shown in c)–d) and g)–h) for the background and sub-storm cases respectively.

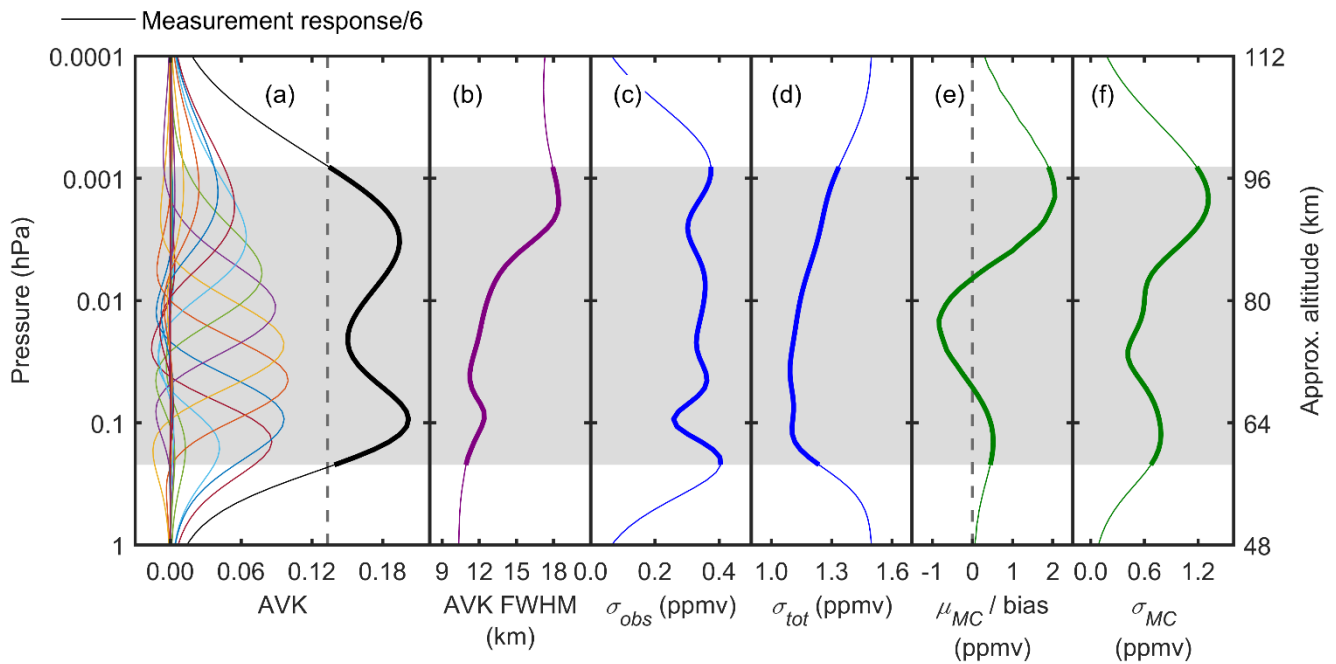


**Figure 9:** Ozone ( $O_3$ ) retrieval diagnostics for simulated 6 h observations of the  $O_3$  11.072 GHz emission line using a ground-based radiometer with 1 mK baseline noise level, 10 kHz frequency resolution, and  $82^\circ$  zenith angle located at Kilpisjärvi ( $69^\circ 03'$  N,  $20^\circ 48'$  E), Finland in clear-sky December conditions. In a) every sixth averaging kernel and the scaled measurement response (MR) are shown. Panel b) shows the full-width half maxima of each averaging kernel (AVK FWHM). The measurement uncertainty ( $\sigma_{obs}$ ) and total uncertainty ( $\sigma_{tot}$ ) are shown in c) and d) respectively. The mean ( $\mu_{MC}$ ) and standard deviation ( $\sigma_{MC}$ ) of the differences between the retrieved and “true” profiles from Monte Carlo (MC) error analysis using 500 repeat inversions are shown in e) and f) respectively. The vertical grey dashed line in a) shows the cut-off for  $MR \geq 0.8$ . The grey shaded regions and the thicker sections of the plotted curves indicate the pressure / altitude ranges where  $MR \geq 0.8$ .

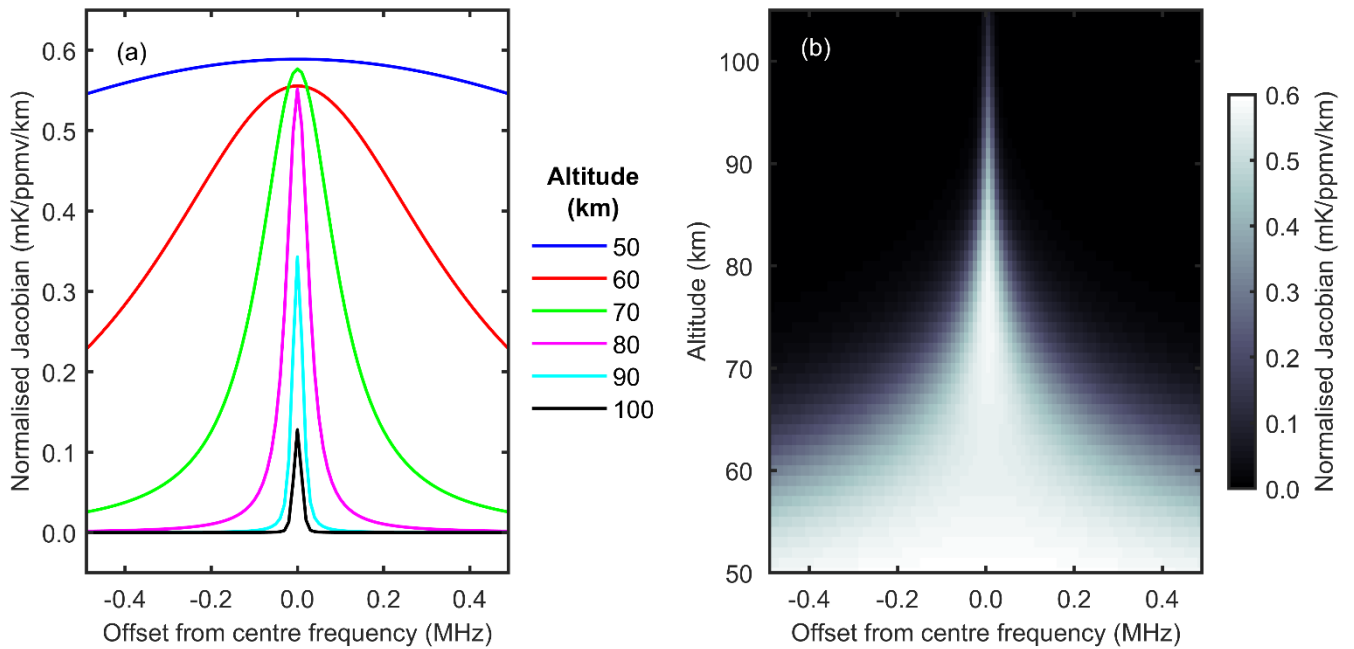
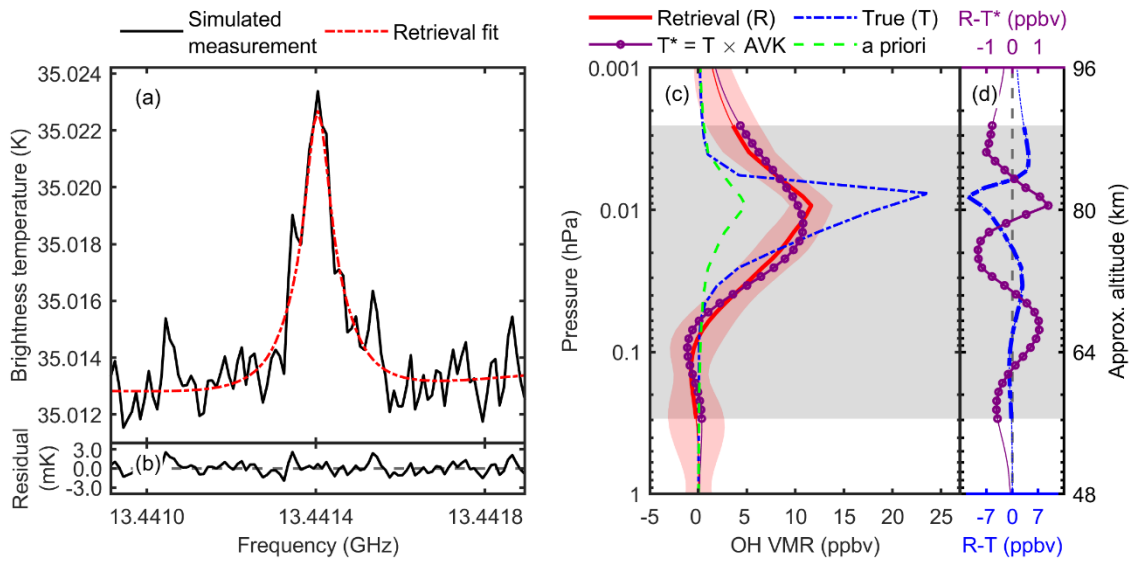


**Figure 10:** Rows of the Jacobian describing the ozone ( $O_3$ ) retrieval, normalised by the layer thickness of the retrieval grid. The data are for retrievals from simulated 6 h observations of the  $O_3$  11.072 GHz emission line using a ground-based radiometer with 1 mK baseline noise level, 10 kHz frequency resolution, and  $82^\circ$  zenith angle located at Kilpisjärvi ( $69^\circ 03'$  N,  $20^\circ 48'$  E), Finland in clear-sky December conditions. Rows of the Jacobian matrix for selected altitude levels are plotted in a). The grey scale in b) indicates the values of the Jacobian matrix.



5 **Figure 11:** Hydroxyl (OH) retrievals for simulated 6 h observations of the OH 13.441 GHz emission line using a ground-based radiometer with vertical sensor polarisation at Kilpisjärvi (69°03' N, 20°48' E), Finland. The forward model clear-sky spectrum is calculated using the model OH profile for substorm conditions in December 2007 with 1 mK baseline noise, 10 kHz frequency resolution, 82° zenith angle, and 0° azimuthal angle (i.e. north-pointing). The simulated OH spectra and retrieval fit are shown in a), and the residual differences in b). The a priori, true, and retrieved OH volume mixing ratio profiles, and the differences between the retrieved and true profiles, are shown in c) and d). Note that the scales differ for the upper and lower axes of d).

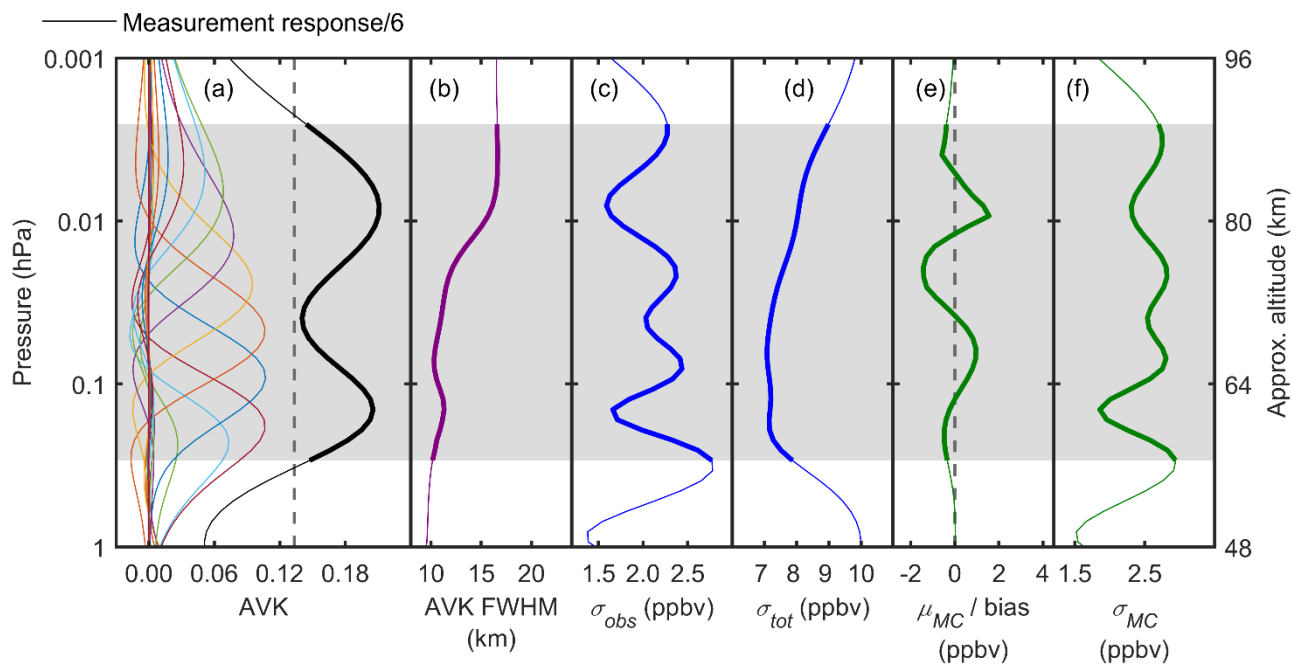


**Figure 12:** Hydroxyl (OH) retrieval diagnostics for simulated 6 h observations of the OH 13.441 GHz emission line using a ground-based radiometer with vertical polarisation, 1 mK baseline noise level, 10 kHz frequency resolution, 82° zenith angle, and 0° azimuthal angle (i.e. north-pointing) located at Kilpisjärvi (69°03' N, 20°48' E), Finland in clear-sky December conditions. In a) every sixth averaging kernel and the scaled measurement response (MR) are shown. Panel b) shows the full-width half maxima of each averaging kernel (AVK FWHM). The measurement uncertainty ( $\sigma_{obs}$ ) and total uncertainty ( $\sigma_{tot}$ ) are shown in c) and d) respectively. The mean ( $\mu_{MC}$ ) and standard deviation ( $\sigma_{MC}$ ) of the differences between the retrieved and “true” profiles from Monte Carlo (MC) error analysis using 500 repeat inversions are shown in e) and f) respectively. The vertical grey dashed line in a) shows the cut-off for  $MR \geq 0.8$ . The grey shaded regions and the thicker sections of the plotted curves indicate the pressure / altitude ranges where  $MR \geq 0.8$ .

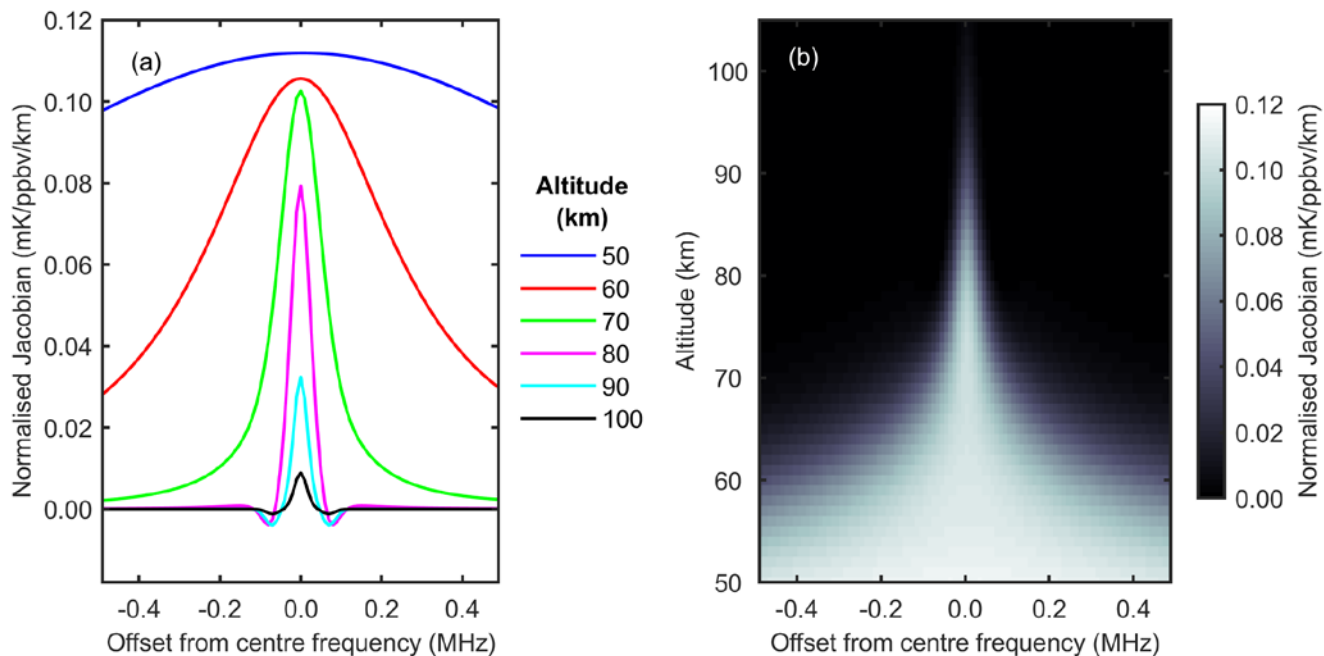


**Figure 13:** Rows of the Jacobian describing the hydroxyl (OH) retrieval, normalised by the layer thickness of the retrieval grid. The data are for retrievals from simulated 6 h observations of the OH 13.441 GHz emission line using a ground-based radiometer with vertical polarisation, 1 mK baseline noise level, 10 kHz frequency resolution, 82° zenith angle, and 0° azimuthal angle (i.e. north-pointing) located at Kilpisjärvi (69°03' N, 20°48' E), Finland in clear-sky December conditions. Rows of the Jacobian matrix for selected altitude levels are plotted in a). The grey scale in b) indicates the values of the Jacobian matrix.